UNIVERSITY OF THESSALY

POLYTECHNIC SCHOOL

DEPARTMENT OF MECHANICAL ENGINEERING

UNIVERSITY OF THESSALY
creative years

Diploma Thesis

Corrosion performance of 2707 Hyper-Duplex Stainless Steel : Cyclic Potentiodynamic Polarization and microstructural characterization.

By

Kleanthis-Konstantinos Karagiannis

Supervisor

Anna Zervaki

Submitted for the Partial Fulfillment

of the requirements for the degree of

Diploma in Mechanical Engineering

2018

Certified by the members of the Thesis Committee :

First examiner   Dr. Anna Zervaki

(Supervisor)   Lab Teaching Staff, Department of Mechanical Engineering,

                        University of Thessaly

Second examiner   Dr. Angeliki Lekatou

(Co-Supervisor)   Professor, Department of Materials Science and

                        Engineering, University of Ioannina

Third examiner   Dr. Alexios Kermanidis

                        Assistant Professor, Department of Mechanical Engineering,

                        University of Thessaly

Acknowledgments

Abstract

Duplex stainless steels (DSS), characterized by a two phase (ferrite and austenite) microstructure, have gained interest in the area of Materials Science thanks to their excellent corrosion resistance and mechanical properties. These advantages have established the prevalence of DSS in various applications, such as petroleum, gas refineries and marine environments. The constant progress in the field contributed to the formation of hyper-duplex stainless steels, like 2707.

The current thesis focuses on the evaluation of the corrosion properties of the newly developed hyper-duplex stainless steel 2707, and specifically its susceptibility to pitting corrosion. The method selected to evaluate this characteristic was cyclic potentiodynamic polarization. This technique has been established, as an extremely reliable accelerated corrosion method for the evaluation of behavior of metals and alloys against corrosion.

To that purpose, specimens of hyper-duplex stainless steel 2707 were properly prepared and tested through the above mentioned corrosion testing method, which was performed in the Department of Materials Science at University of Ioannina. The characterization work conducted at University of Thessaly, included the preparation of the specimens as well as the characterization of the corrosion mechanism, evolved during the tests. Stereo – Optical microscopy, SEM, EDX, ICP and XPS analyses were employed in the evaluation process.

The corrosion rate was a crucial result, extracted from this analysis, as this kind of procedure simulates with great accuracy the exposure of the alloy in the desired corrosive environment. The environment selected for this study was a 3,5% wt NaCl solution, which represents sea water.

The corrosion mechanism was defined and, furthermore, the products of corrosion were identified. Also, polarization curves describe in great detail the susceptibility of the specimen to pitting corrosion. Results of all the analyses, that were conducted, indicated the differentiation of corrosion resistance behavior between the two phases of the hyper duplex 2707 stainless steel. The ferritic phase proved to be more prone to corrosion.

The results are in good agreement with the reported values found in the open literature.

Περίληψη

Οι διφασικοί ανοξείδωτοι χάλυβες διαθέτουν χαρακτηριστική μικροδομή που αποτελείται από φερρίτη και ωστενίτη. Αυτή η οικογένεια χαλύβων κερδίζει συνεχώς έδαφος στο τομέα της Επιστήμης των Υλικών χάρη στις αξιοσημείωτες διαβρωτικές και μηχανικές τους ιδιότητες. Αυτά τα πλεονεκτήματα έχουν εδραιώσει την κυριαρχία των διφασικών ανοξείδωτων σε ποικίλες εφαρμογές, όπως η πετρελαϊκή βιομηχανία και η χρήση σε υδάτινα περιβάλλοντα. Η διαρκής πρόοδος σε αυτό τον τομέα συνείσφερε στη δημιουργία των υπέρ-διφασικών ανοξείδωτων χαλύβων, όπως ο 2707.

Η παρούσα διπλωματική επικεντρώνεται στην επαλήθευση των εξαιρετικών διαβρωτικών ιδιοτήτων του υπέρ-διφασικού ανοξείδωτου χάλυβα 2707, και ιδιαιτέρως στην επιδεκτικότητά του σε διάβρωση οπών. Οι μέθοδος που επιλέχθηκε για την εξακρίβωση αυτού του χαρακτηριστικού είναι η κυκλική ποτενσιοδυναμική πόλωση. Αυτή η μέθοδος έχει εδραιωθεί τα τελευταία χρόνια ως μια ιδιαίτερα ακριβής μέθοδος επιταχυνόμενης διάβρωσης για τη διερεύνηση της συμπεριφοράς μετάλλων και κραμάτων σε διαβρωτικά περιβάλλοντα.

Για αυτό το σκοπό, δοκίμια του υπέρ-διφασικού ανοξείδωτου χάλυβα 2707 προετοιμάστηκαν κατάλληλα και εξετάστηκαν μέσω της προαναφερθείσας μεθόδου, η οποία πραγματοποιήθηκε στο τμήμα Επιστήμης των Υλικών του Πανεπιστημίου Ιωαννίνων. Η ανάλυση των πειραματικών αποτελεσμάτων διεξήχθη στο τμήμα Μηχανολόγων Μηχανικών του Πανεπιστημίου Θεσσαλίας και περιελάμβανε την προετοιμασία των δοκιμίων, καθώς και τον χαρακτηρισμό του μηχανισμού διάβρωσης, ο οποίος έλαβε χώρα κατά τη διεξαγωγή των πειραμάτων που περιγράφηκαν. Για την επίτευξη αυτών των στόχων πραγματοποιήθηκαν στερεοσκοπική και μικροσκοπική παρατήρηση, καθώς επίσης αναλύσεις SEM, EDX, ICP και XPS.

Ο υπολογισμός του ρυθμού διάβρωσης αποτέλεσε σημαντικό στοιχείο, το οποίο εξήχθη από την ανάλυση των πειραματικών αποτελεσμάτων, καθώς η παρούσα δοκιμή διάβρωσης προσομοιώνει με μεγάλη ακρίβεια την έκθεση του κράματος στο επιθυμητό διαβρωτικό περιβάλλον. Το περιβάλλον που επιλέχθηκε στην παρούσα εργασία ήταν ένα διάλυμα χλωριούχου νατρίου 3,5% κ.β., το οποίο προσομοιώνει του θαλασσινό νερό.

Η μηχανισμός της διάβρωσης καθορίστηκε και επιπλέον ταυτοποιήθηκαν τα προϊόντα της διάβρωσης. Επίσης οι καμπύλες πόλωσης περιγράφουν λεπτομερώς την επιδεκτικότητα του δοκιμίου στη διάβρωση οπών. Τα αποτελέσματα όλων των αναλύσεων που πραγματοποιήθηκαν υποδεικνύουν διαφοροποίηση της διαβρωτικής συμπεριφοράς των δύο φάσεων του υπέρ-

διφασικού ανοξείδωτου χάλυβα 2707. Η φάση του φερρίτη αποδεικνύεται πιο επιδεκτική σε διάβρωση.

Τα αποτελέσματα των πειραμάτων κυκλικής ποτενσιοδυναμικής πόλωσης, καθώς και ο μηχανισμός διάβρωσης του υπέρ-διφασικού ανοξείδωτου χάλυβα, συμφωνούν με αντίστοιχα αποτελέσματα που αναφέρονται στη βιβλιογραφία.

Table of Contents

List of Figures

List of Tables

Chapter 1 : Introduction

1.1 Aim and Structure of the Diploma Thesis

The aim of this work is to determine the severity of pitting corrosion, in specimens of hyper duplex 2707 steel through cyclic potentiodynamic polarization in 3,5 % NaCl solution. The corrosion environment simulates the seawater.

The thesis consists of five chapters, which are briefly presented below.

In Chapter One, general information about duplex stainless steels and also definition of corrosion in metals and its respective types are given.

In Chapter Two, literature review is presented. In the review a presentation of different materials, that were widely used in corrosive environments, is provided. A comparison between these materials and the hyper-duplex 2707 takes place and demonstrates the superiority of this super-duplex stainless steel in corrosion resistance.

In Chapter Three, the experimental procedure is described.

In Chapter Four, the results of cyclic potentiodynamic polarization method, ICP analysis of the NaCl solution collected after the experiments, optical and stereo microscopy studies and also SEM/EDX and XPS analyses are presented.

In Chapter Five, the above results are discussed in order to define the resistance of the super-duplex steel 2707 against pitting corrosion and also describe the corrosion mechanism. At the end, some future work recommendations are provided.

1.2 Corrosion in metals

Corrosion in metals can be defined as the deterioration of their structure due to specific reactions with the environment. The severity of corrosion depends on several factors including the chemical composition, and the microstructure of the exposed material, and also the surrounding environment, with gasses and chlorine-rich environments to be considered as most corrosive. Corrosion is considered as an electrochemical reaction, which consists of redox reactions. As a matter of fact, flow of electrons is needed and steels are conductive materials, which makes them prone to corrosion. The basic factors that define the corrosion of steels are :

- Chemical composition and microstructure of metal
- Chemical composition of the environment
- Natural factors, as the temperature, radiation, etc.
- Mechanical stresses on the material (e.g. tension stress, shock or friction)

Another factor that plays a crucial role in the initiation and the progress of the corrosion is the shape and the morphology of the material. In case of a surface abnormality the possibility for corrosion is higher.

During the redox reactions, one atom or ion loses one or more electrons (oxidation) and another one receive them (reduction). For example, if a piece of steel is exposed to rainwater (dissolved oxygen) the following reactions will occur [1]:

$$\text{Anodic reaction (oxidation) : } Fe \rightarrow Fe^{2+} + 2e^- \quad (1.1)$$

$$\text{Cathodic reaction (reduction) : } H_2O + \tfrac{1}{2} O_2 + 2e^- \rightarrow 2OH^- \quad (1.2)$$
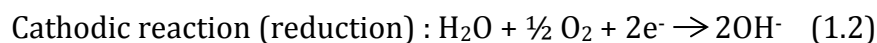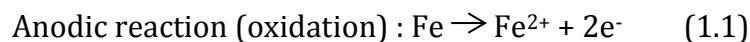
Those two reactions happen at the same time, with the same rate. The total electrochemical reaction can be written as :

$$Fe + \tfrac{1}{2} O_2 + H_2O \rightarrow Fe^{2+} + 2OH \quad (1.3) \text{ or}$$

$$2Fe + O_2 + 2H_2O \rightarrow 2Fe(OH)_2\downarrow \quad (1.4)$$
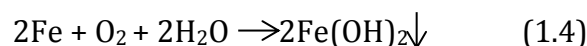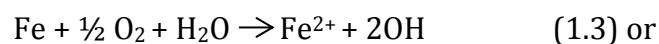
At the second stage the bivalent iron oxidizes to triacetate according to :

$$4Fe(OH)_2 + O_2 + 2H_2O \rightarrow 4Fe(OH)_3 \quad (1.5)$$
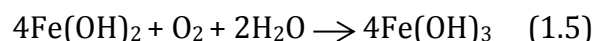
Finally, the dehydration of hydroxide leads to the formation of red or brown rust on the surface of the metal. The following reaction depicts the formation of the hydrate iron oxide ($2Fe_2O_3 . H_2O$) :

$$4Fe(OH)_3 \longrightarrow 2Fe_2O_3 + 6\ H_2O \qquad (1.6)\ or$$

$$4Fe(OH)_2 + O_2 \longrightarrow 2\ H_2O + 2Fe_2O_3.\ H_2O \qquad (1.7)$$
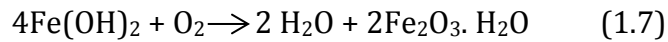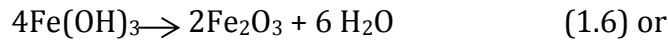
1.3 Types of corrosion

There are nine types of corrosion of metallic specimens, as shown in figure 1. [2]

- Uniform corrosion : It is the simplest type of corrosion. The whole surface of the metallic specimen or a big part of the surface is attacked and as a result a uniform mass loss is noticed.
- Galvanic corrosion : It happens when two dissimilar metals are in contact with each other and with an electrolyte (e.g. water or other solution). Then a galvanic cell is set up and the corrosion is accelerated.
- Crevice corrosion : It is one of the most common type of corrosion. The cause of this phenomenon is the variance of oxygen concentration on the surface of a metal, allowed by crevices or narrow openings.
- Pitting corrosion : Also a very common and severe type of corrosion. The passive layer on steel, which protects it against corrosion, can be attacked by specific chemical species, especially chloride ion Cl^-. As a result, a lot of pittings are formed on the surface of the metal, which can lead to perforation of the specimen or make it prone to different types of corrosion.
- Intergranular corrosion : In case of a steel with high carbon level, chromium may combine with carbon and form chromium carbides at a temperature range of 450-850°C. This process is also called sensitization and usually happens during heat processes, such us welding and solidification.
- Selective corrosion – De-alloying : It is about the selective dissolution of the elements in a single phase alloy or one of the phase in a multiphase alloy.
- Erosion corrosion : A degradation of metal surface takes place, due to a combination of an electrochemical reaction and a mechanical action, often by mechanical friction or due to impact with liquid or gas.
- Stress corrosion cracking : It requires a combination of tensile stress, temperature and corrosive environment. As a result, cracks appear at stresses far below the tensile stress of the steel.
- Biological corrosion : Living microorganisms may cause the initiation of corrosion. The digestive activities of these organisms can lead to

degradation of the metal, due to the formation of a corrosion-friendly environment.
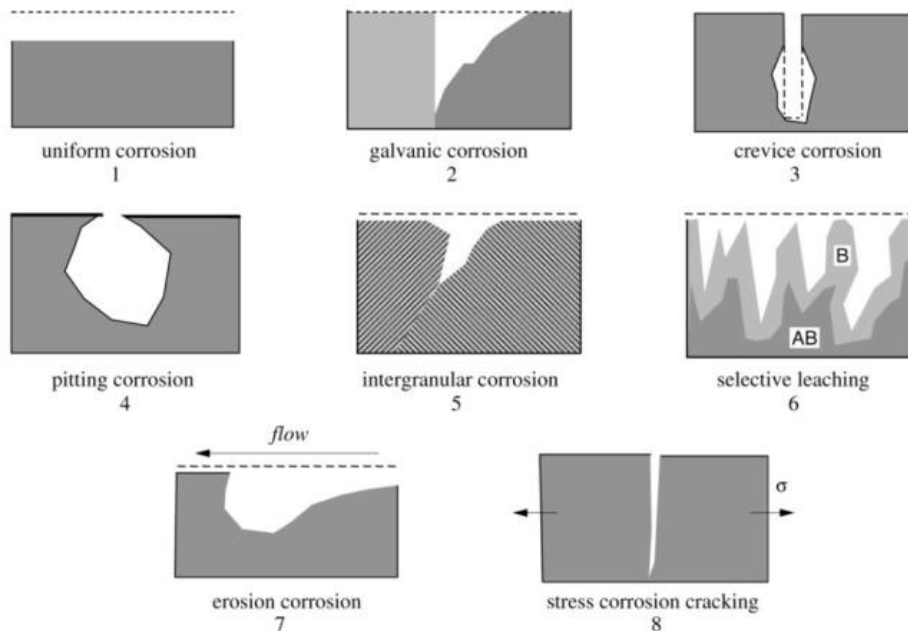
This study will mainly focus on pitting corrosion, that occur on duplex stainless steels. This type of corrosion causes the formation of pittings with small diameter on the surface of the metal. Therefore, the size pitting may enlarge going deeper in the specimen. It is considered as the worst type of corrosion as it progresses unexpectedly and can lead to catastrophic failure of the metal.

1.4 Duplex Stainless Steels (DSS)

Duplex Stainless Steels cover a wide field of applications, where good corrosion resistance is needed. Microstructure of DSS consists of austenite and ferrite in roughly equal proportions, so they combine good mechanical properties and excellent corrosion resistance. This thesis will focus on the properties of Super-Duplex Stainless Steel (SDSS) 2707. Some special characteristics of this steel are [4] :

- Excellent resistance to pitting and crevice corrosion
- Excellent resistance to stress corrosion cracking
- High resistance to general corrosion
- Excellent resistance to erosion corrosion
- Excellent corrosion fatigue properties

- Extremely high mechanical strength
- Physical properties that offer design advantages
- Good weldability

Chapter 2 : Literature Review

2.1 Stainless steel (SS)

There has been a continuous need for materials that could be used in applications with corrosive environments. The first ever patent that could be considered as stainless steel was that established by Woods and Clark in 1872 [5]. They produced an iron alloy which contained 30-35% Cr and 2% W. But it wasn't until 1875, when the importance of low carbon, for the production of stainless steel, was noticed by Brustlein. He declared that in order to achieve high percentage of Cr in an alloy, C content must drop at around 0.15%. Two decades later, in 1895, Hans Goldschmidt developed the aluminothermic reduction process for producing carbon-free chromium, which made the production of SS feasible. In 1906 Leon Guillet made an extended analysis on Fe-Ni-Cr alloys, which can be considered as the basis of 300 series. In 1909, Albert Portevin, conducted a thorough study on the today called 430 SS. An important step for the progress of SS was made in 1911 by P. Monnartz and W. Borchers. They found the lower limit of Cr content in an alloy, in order to acquire a remarkable resistance against corrosion (10,5%) and also studied the behavior of Mo towards this direction. The most significant moment for SS is settled in 13th August 1913, when Harry Brearley created a steel with 12,8% Cr and 0,24% C. This alloy is argued to be the first ever stainless steel.

Since then a huge progress has been achieved in this field and various types of stainless steels have been manufactured. In correspondence with their microstructure SS are listed in the following categories :

- Ferritic SS with Cr content at 10,5%-30% wt and C content (≤0,2% wt).
- Martensitic SS with Cr content at 10,5%-17% wt and C content (≤1,2% wt).
- Austenitic SS with Cr content at 17%-25% wt, Ni at 7%-35% wt and C content 0,03%-1,1% wt.
- Duplex SS (DSS) with Cr at 23%-30% wt, Ni at 2%-7% wt and small additions of Ti and Mo. The two phases are austenite and ferrite.
- Precipitation hardened steels that include tiny quantity of elements like Cu, Al or Ti in order to get hardened through precipitation.

It is possible for some types of stainless steels to consist of high Cr (≥30% wt) or low Fe content (≤50% wt) [5].

2.2 Duplex Stainless Steel (DSS)

This study will focus on a specific type of SS, the duplex SS, which arise as a very promising material for applications that acquire high corrosion resistance. Duplex stainless steels are so-called because of their dual-phase microstructure of austenite and ferrite. The history of DSS begins back to 1930, when the first wrought DSS was produced in Sweden [6] and used in the sulfite paper industry. This type of steel came in the foreground in order to confront the intergranular corrosion problems faced with early high-carbon austenitic SS. In 1930 first duplex casting were produced in Finland and in 1936 French scientists developed the well-known AISI Type 329. Unfortunately, some difficulties were met during the welding of these materials. The heat-affected zone (HAZ) showed extremely lower corrosion resistance in correlation with the base metal. Luckily, in 1968, the invention of argon oxygen decarburization (AOD) process offered the opportunity to add nitrogen as an alloying element, thus the stability of austenite was increased. A remarkable period of progress in the field of DSS was due to the development of offshore gas and oil fields in the North Sea, where huge amounts of SS with great chloride corrosion resistance were needed. It was the time when DSS 2205 made its debut and established its superiority.

It wasn't until early nineties when great progress in wrought and forged products was made and as a result improvement of mechanical properties and corrosion resistance was achieved. The fruit of this progress were the today called super-duplex stainless steels (SDSS). The first SDSS to be manufactured were those with grade such as UNS S39550, S39750 and S39760. Except of the significant properties and despite the fact that they consist of huge proportions of alloying elements, SDSS have to demonstrate an unexpected low cost thanks to their low content (<5%) of Ni, which is one of the most expensive alloying elements [7]. Nowadays, modern stainless steels have been divided into five groups, according to their corrosion resistance :

- Lean duplex without deliberate Mo addition (e.g. 2304).
- Molybdenum lean duplex (e.g. S32003).
- Standard duplex with chromium (Cr) content at 22% wt and molybdenum (Mo) content at 3% wt (e.g. 2205).
- Super duplex with Cr content at 25% wt and Mo content at 3% wt (e.g. 2507).
- Hyper duplex with higher Cr and Mo contents than SDSS (e.g. 2707 and 3207).

2.3 Corrosion Resistance

The most catastrophic type of corrosion, as far as DSS, is pitting corrosion due to its unexpected rate of evolution and the damage that can cause. So, it is crucial to know, before the application, the possible pitting corrosion resistance of such materials. Also, it would be helpful to simulate the condition, which this material will face during usage, and record its behavior. A first important indication of good pitting corrosion resistance is the PREN value, which depends on the alloying elements of the steel. Furthermore, a well-trusted method for simulating real corrosive conditions is the cyclic potentiodynamic polarization, which gives significant information for crevice and pitting corrosion behavior of the examined material.

2.3.1 PREN value

The resistance of a stainless steel to localized corrosion is closely related to its alloy content. Elements that play a crucial rule are chromium (Cr), molybdenum (Mo), Tungsten (W) and nickel (Ni). An empirical relationship called the Pitting Resistance Equivalent Number (PREN) has been developed and connects the content of stainless steel in alloying elements with its pitting resistance in chloride containing solutions. The PREN relationship for austenitic and duplex stainless steels is the following :

$$\text{PREN = Cr + 3,3 (Mo + 0,5W) + 16N} \qquad (2.1)$$

where element content is used in weight %.

In order to assume that a type of steel is chloride resistant the PREN value must exceed 40 [7]. Three widely used super-duplex stainless steels are 2505, 2707 and 3207 with respective minimum PREN values 41, 48 and 50.

2.3.2 Pitting corrosion testing

There is a variety of methods able to determine the resistance of a steel grade to pitting. The toughest pitting corrosion test is ASTM G48, where Method A is used to determine the relative pitting resistance of SS and nickel-base, chromium-bearing alloys at one temperature and Method E categorizes alloys by critical pitting temperature (CPT) which indicates the initiation of pittings and propagation to a visibly detectable size in a standard ferric chloride solution. Additionally, for high-alloy grades, corrosion testing described by ASTM G150 in

the neutral solution of 1M NaCl is very common [4]. Similarly, this critical temperature appears as far as crevice corrosion and is called critical crevice temperature (CCT). Finally, another efficient way to evaluate the pitting corrosion behavior of an alloy would be the cyclic potentiodynamic polarization and, furthermore, potentiostatic and potentiodynamic anodic polarization measurements. These tests are conducted according to ASTM G5-94(2011), G71-81(2014) and G61-86(2014). This thesis include the cyclic potentiodynamic polarization measurements from the hyper-duplex stainless steel 2707, that will be shown on Chapter 3.

2.4 Hyper-Duplex 2707 and its competitors

It has been a long period of time, while the austenitic stainless steels 304L and especially 316L have been used in applications including corrosive environments (e.g. seawater, acidic mixtures). The constant need for better performance brought to the foreground new materials like super-austenitic stainless steels, super and hyper-duplex stainless steels. Various studies declared the superiority of these steel grades over 304L and 316L [8],[9]. Additionally. comparison among these hyper-materials will indicate the suitable one for each corrosive environment.

A first and general aspect in order to classify materials as far as their susceptibility to pitting corrosion would be the PREN value, which depends only on the content of the alloying elements. Table 1 shows the chemical composition and PREN for a range of austenitic and duplex stainless steels [4] :

Table 1 : Chemical composition and PREN of common austenitic and duplex stainless steels [4]

Grade	304L	316L	2205	2507	2707
UNS No.	S30403	S31603		S32750	S32707
C	0,03	0,03	0,03	0,030	0,03
Cr	17,5-19,5	16,0-18,0	22,0	25	27
Ni	8,0-12,0	10,0-14,0	5	7	6,5
Mo	-	2,0-3,0	3,2	4	4,8
N	0,10	0,10	0,18	0,3	0,4
Mn	2,00	2,00	2,0	1,2	1,5
Cu	-	-	-	-	-
Co	-	-	-	-	1,00
Si	-	-	1,0	0,8	0,5
S	-	-	0,015	0,015	0,010

P	-	-	0,03	0,025	-
PREN	18-19	24-25	35	41	48

Table 1 indicates the increase of PREN as alloying elements like Mo and N are added. Wherever there is a single value and not a value range, this represents the minimum alloying element content.

Several studies have been made in order to compare duplex SS with other steel grades used in corrosive environments. It is useful to compare the susceptibility of a stainless steel to pitting corrosion by recording the respective CPT. Such a survey compares CPT and CCT values of austenitic SS and duplex SS in accordance to ASTM G48 (Figure 2) [6].
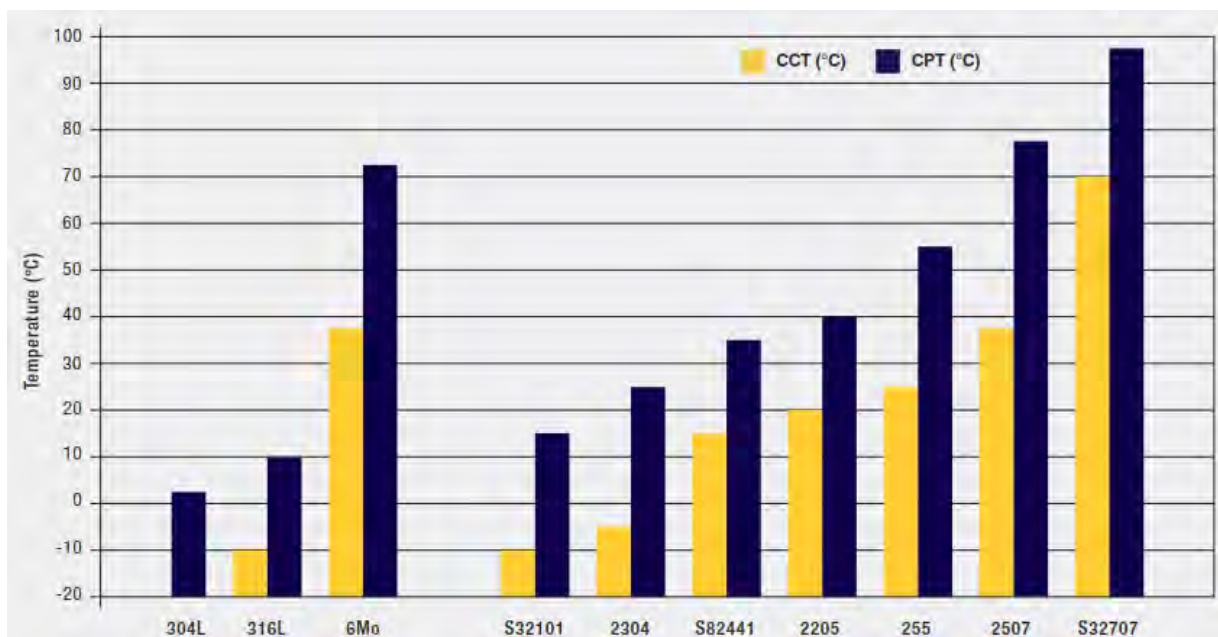
Figure 2 : Critical pitting and crevice corrosion temperatures for unwelded austenitic (left) and duplex (right) stainless steels [6].

CPT of duplex stainless and especially of 2205, 2507 and 2707 is well above 316L, which make them preferable in applications in Cl-rich environments. It is obvious that the highly alloyed duplex SS exhibit the higher CPT.

It was made clear, from Table 1, that DSS 2507 and 2707 show significant pitting corrosion resistance. In more detail, Figures 3 and 4 provide a comparison between these two grades. [4]
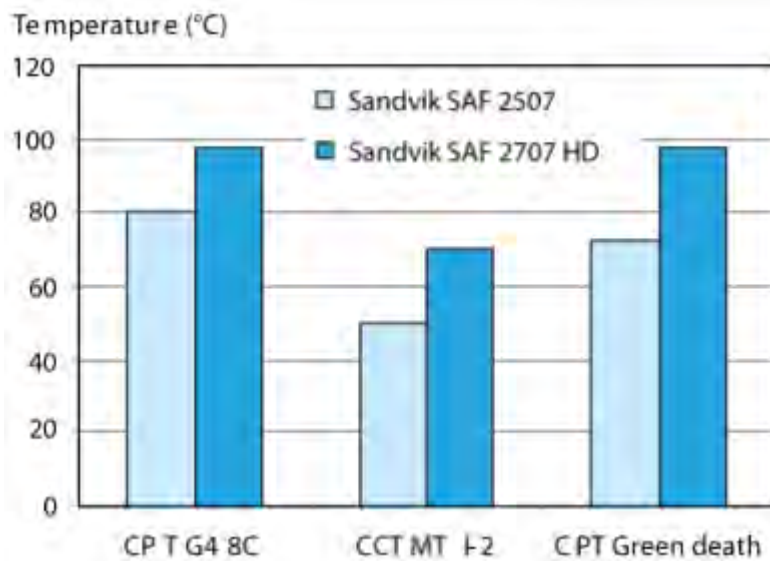
Figure 3 : Critical pitting temperature measured as proposed by ASTM G48C and Green death, also CCT measured as proposed by MTI-2. [4]

The hyper-duplex 2707 shows superior corrosion resistance in comparison to 2507.
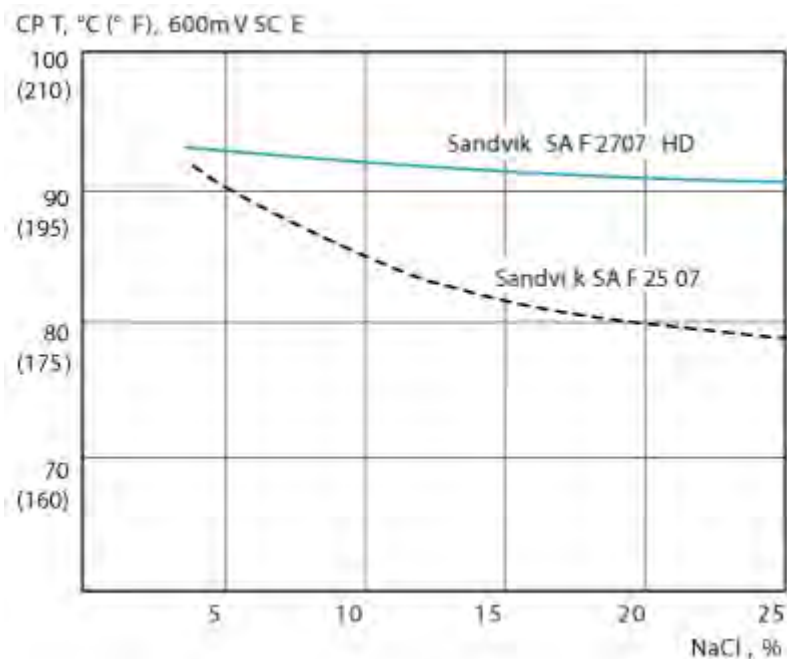
Figure 4 : Critical pitting temperature at varying concentrations of sodium chloride. [4]

Figure 4 shows the stability of CPT of 2707 even at higher concentrations of NaCl. By contrast, 2507 is proved to be inferior, as its CPT drops.

Another comparative study confirmed that the CPT of 2707 is close to 100°C according to ASTM G48 [10]. A useful diagram was constructed and showed the correlation between CPT and PREN (Figure 5). It can be assumed that the resistance to pitting is mostly governed by the chemical composition and is almost independent on the structure.
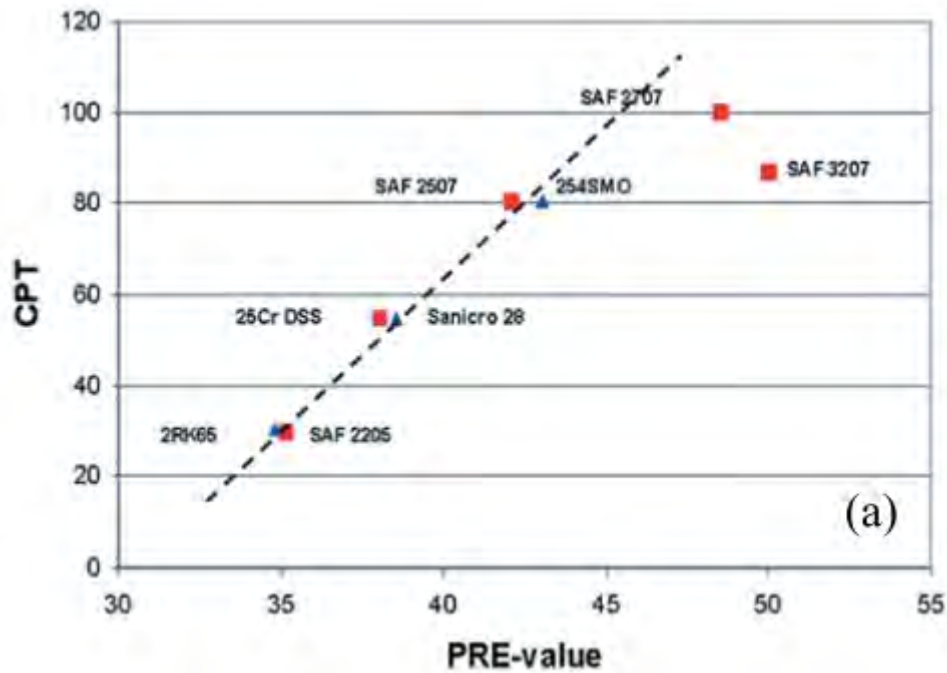
Figure 5 : Correlation between CPT and PREN. [10]

An analytical comparable study between such materials has been published by Bellezze et al. [5], [6] This study compared two super-austenitic SS, AISI 904L and Sanicro 28, two super-duplex SS, SAF 2205 and SAF 2507, and one hyper-duplex SS, SAF 2707 in an acid mixture containing tartaric acid saturated solution H_2SO_4 and HCl as a function of temperature (22-60°C) and alloys composition. It was proved that the two super-austenitic SS and, also, the hyper-duplex SS are good alternatives of 316L in the industry plant, where tartaric acid was produced. In order to reach this conclusion cyclic potentiodynamic polarization experiments were conducted and the results are given in Fig. 6 [5],[6] :
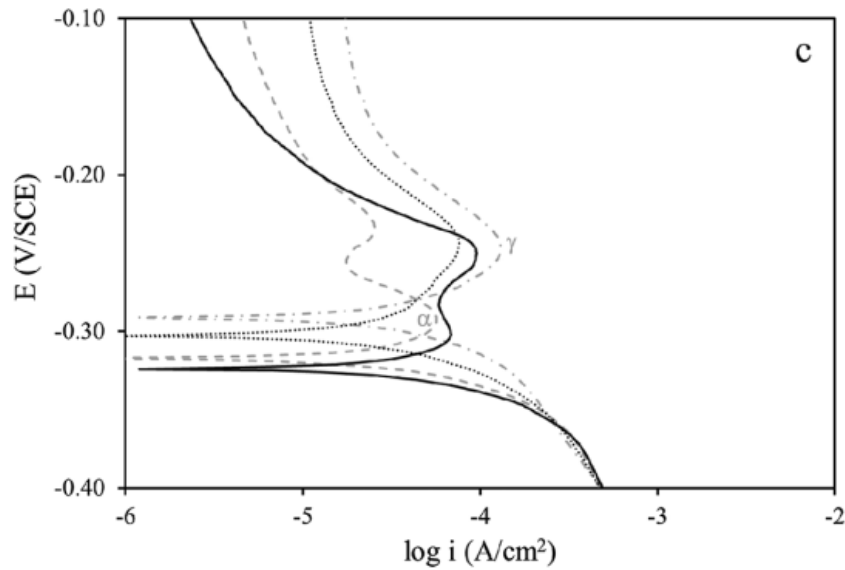
Figure 6 : Anodic polarization curve of 2707 alloy in tartaric acid saturated solution H$_2$SO$_4$ and HCl at 40°C. ___ experimental curves, ... calculated curves, --- experimental curves obtained with α electrodes, _ . experimental curves obtained with γ electrodes [5], [6]

In this case, a different behavior can be observed between the two phases of the hyper-duplex SS. This phenomenon has been defined as selective corrosion, and more specifically the ferritic phase (α) was found to be more active than the austenitic phase (γ). Due to this abnormality, corrosion consumes the α phase and surrounds the γ phase until its detachment. The above described situation is more common in SAF 2205 where selective corrosion becomes general, and SAF 2507, while SAF 2707 is influenced in smaller extent.

The complication described above is attributed to the preference of Cr and Mo to be partitioned in the ferrite phase, while N prefers austenite [11]. This phenomenon, leads to differences between the PREN values of these two phases, thus susceptibility to pitting corrosion is different. It is possible to bypass this abnormality through annealing at a specific temperature, where PREN of both phases equalizes. Soon-Hyeok Jeon *et al.* [12] studied the effects of solution annealing conditions on the precipitation of secondary phases and the pitting corrosion resistance after aging at 1123 K. Because of the high content in Cr and Mo, precipitation of secondary phases is very common in hyper-duplex SS and it happens more frequently into the ferritic phase. These phases reduce the fracture toughness and the pitting corrosion resistance of the steel. This is the main reason why ferritic phase is more prone to pitting corrosion in comparison to the austenitic.

In this study, potentiodynamic curves were constructed for various annealing temperatures and aging times. (Figures 7 & 8)
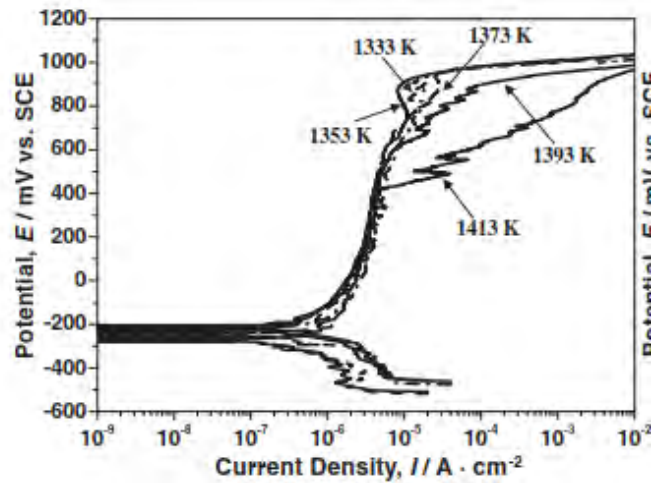
Figures 7 : Potentiodynamic curves in 4M NaCl solution at 343 K after solution heat treatment at different temperatures for 30 min [12]
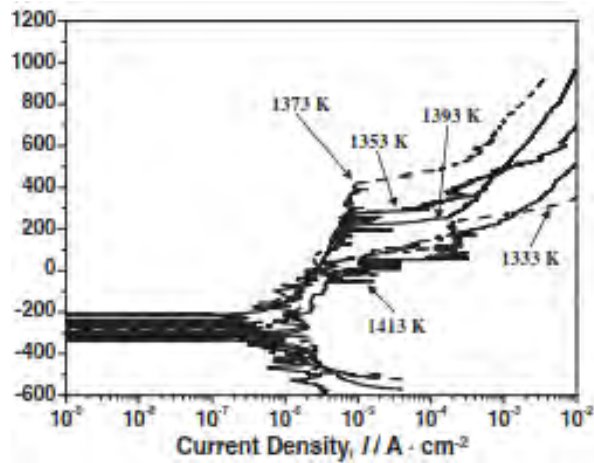
Figure 8 : Potentiodynamic curves in 4M NaCl solution at 343 K after aging at 1123 K for 10 min. [12]

One way to separate the conditions that lead to better corrosion performance is by comparing the respective pitting potentials. Pitting potential is defined as the breakdown potential, where passive film is destroyed. In Figure 7 the sequence from the most pitting resistant to the least resistant is the following : 1333K=1353K=1373K > 1393K > 1413K. In Figure 8 the corresponding sequence is the following : 1373K > 1353K > 1393K > 1333K > 1413K. Furthermore, PREN values were calculated in each phase with two methods. The first one used the alloying elements compositions shown by EDX analysis, while the second one was based on thermodynamic calculations performed by Thermo-Calc [12]. The results are depicted in Figure 9 :
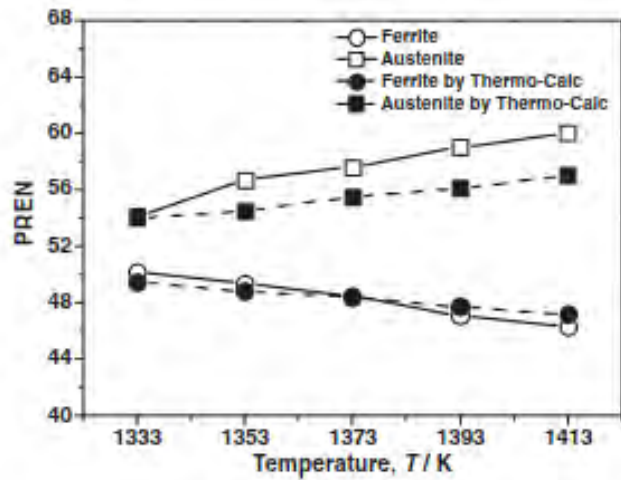
Figure 9 : Effect of solution-annealing temperature on PREN of ferritic and austenitic phases. [12]

This figure shows the increase of PREN difference between the two phases as the annealing temperature gets higher. An acceptable difference would be the one until annealing at 1373K. The results, which indicate the perfect annealing temperature, in order to achieve equal PREN values, are shown in Figure 10.
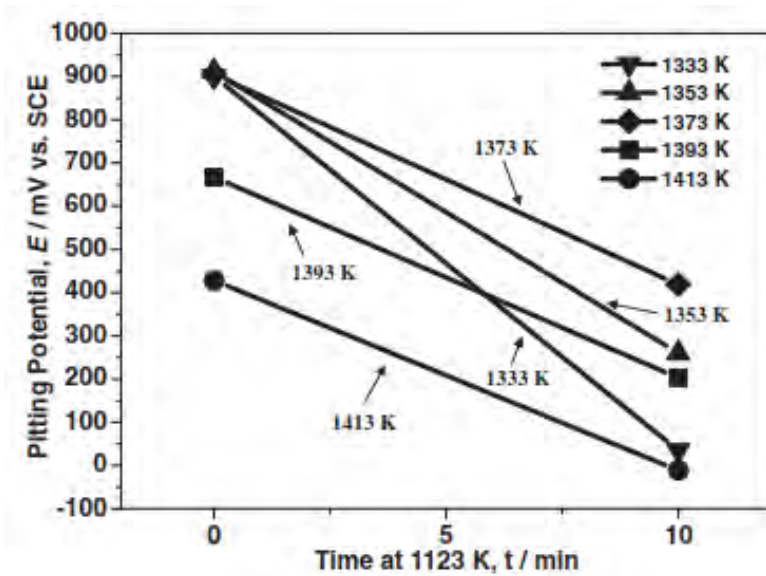
Figure 10 : Effect of solution-annealing temperature and aging time on the pitting potentials [12]

Figure 10 was based on potentiodynamic polarization in 4M NaCl solution at 343K. It shows that the only pitting potential that stays relatively stable with increase of time is that of the specimen annealed at 1373K. Through these figures, the study concluded that the optimum annealing temperature, which solves the selective corrosion problems arising by unequal PREN values of ferritic and austenitic phases, is 1373K.

Chapter 3 : Experimental Procedure

3.1 Preparation of specimens

Within this study, specimens of the hyper-duplex SS 2707 were examined in order to determine their susceptibility to pitting corrosion.

The material belongs to hyper-duplex stainless steel family and its composition is shown in the following table :

Table 2 : Chemical composition of hyper-duplex SS 2707

Grade	UNS No	C	Cr	Ni	Mo	N	Mn	Co	Si	S
2707	S32707	0,03	27	6,5	4,8	0,4	1,5	1,00	0,5	0,010

The PREN, calculated with equation (2.1), is 48, which indicates high pitting corrosion resistance.

For the corrosion tests, cutting, grinding and polishing had to be made in order to prepare the proper shape and surface quality for the cyclic potentiodynamic polarization tests. The material was delivered as a tube with 2cm diameter, so it was necessary to be cut in longitudinal and transverse direction as depicted in Figure 11. Cutting was performed with Struers ''Accutom 2''.

Figure 11 : Initial and final form of specimen

The outer surface of the specimens was grinded with SiC papers 120, 320, 500, 800, 1000 and 2000 grit and then polished with 3μm and 1μm diamond paste. Specimens were mounted in PTFE (Polytetrafluoroethylene) and sealant tape with the addition of a wire in order to be properly prepared for the following corrosion tests. In order to determine the good connection between the specimen and the wire, a voltmeter was used. If the resistance between specimen and wire was close to zero, then the connection was acceptable.
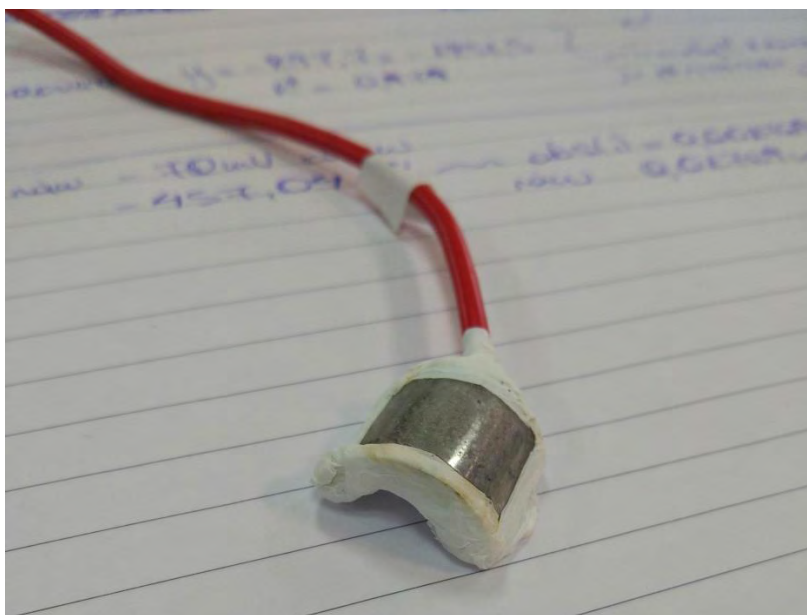
Figure 12 : Specimen just before cyclic potentiodynamic polarization

3.2 Cyclic Potentiodynamic Polarization (CPP)

This type of corrosion testing is typical and simulates the exposing conditions of this steel grade in the respective solution. In this study both surfaces of 2707 specimens were tested in cyclic potentiodynamic polarization in aerated 3,5 % wt NaCl solution. The device used for the electrochemical measurements is the galvanostat-potentiostat Gill AC 1044 from ACM Instruments (Figure 13) in combination with the respective software.

Figure 13 : Galvanostat-potentiostat from ACM Instruments.

The galvanostat adjusts the polarized current automatically in order to control the potential between the active electrode (WE) and the reference electrode (RE). This device changes the potentila with a stable rate and records the current density penetrating the electrochemical cell. The anodic reaction has the following form (3.1) :

$$M \longrightarrow M^{n+} + ne^{-} \qquad\qquad (3.1)$$

The test setup is shown in the following Figure 14:
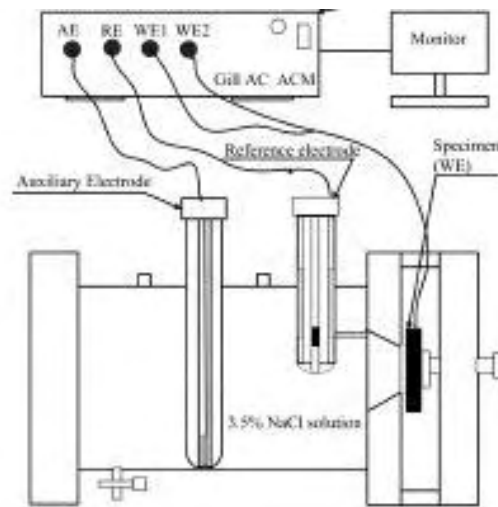
Figure 14 : Test setup

The working electrode (WE) is the specimen that is being examined, 2707 in this case. The reference electrode (RE) was an Ag/AgCl electrode, which is contained into a glass tube, that has a glass porous cap on the down side (Figure 15). The inner wire is maintained in saturated KCl solution. All the measured potentials are calculated in relation to reduction potential of Ag/AgCl ($E_{AgCl} = E_{SHE} + 200$ mV)

Figure 15 : Ag/AgCl reference electrode (RE)

As auxiliary or counter electrode (AE), a platinum (Pt) electrode was used (Figure 16). This type of electrode is very common in corrosion tests according to ASTM G5-94 and G61-86. This type of electrodes should be maintained in a 3M KCl solution in order to avoid diffusion of KCl from the interior of the electrode.

Figure 16 : Auxiliary or counter platinum (Pt) electrode

The electrolyte used was an aerated 3,5% NaCl solution at room temperature (25°C), which simulated seawater conditions. Distilled water was used in order not to influence solution's conductivity. Also, buffer solution was used in irder to keep the solution pH at 7.

All the measurements were conducted according to ASTM G5-94 (2004), ASTM G61-86 (2014) and ASTM G71-81 (2014). The exposed surface was in a range of 1,64-2,62 cm^2. The experimental set up is shown in Figure 17.
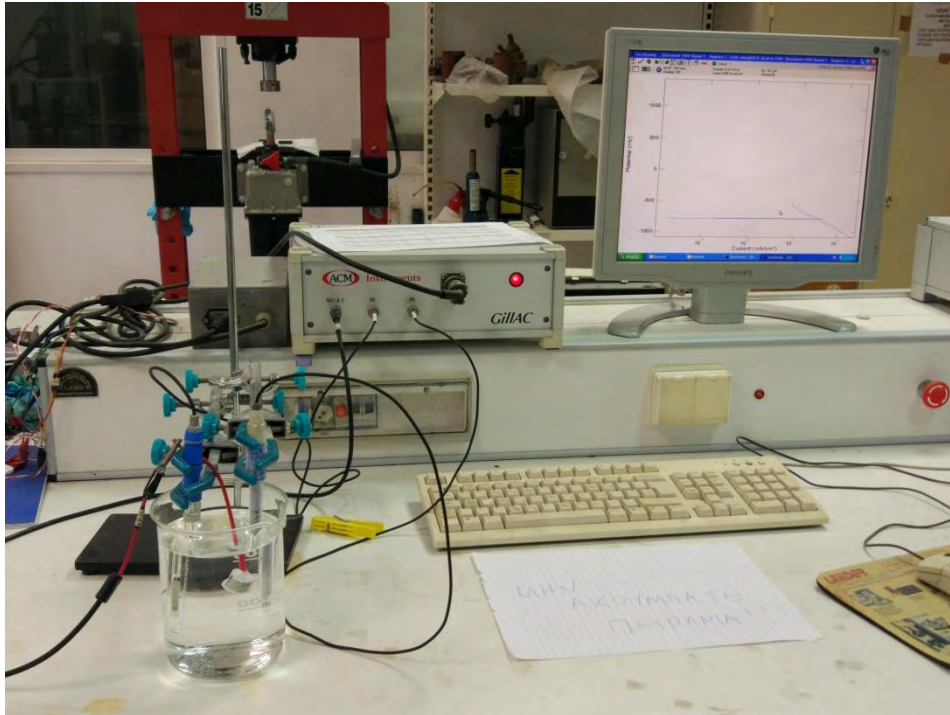
Figure 17 : Experimental set up

The parameters fixed for the cyclic potentiodynamic polarization tests are the following :

- Open circuit equilibrium time : 2 hours
- Potential range : -1500 mV up to +1500 mV as to E_{rest}.
- Scan rate : 10 mV/min.

The polarization test starts with a 2 hour equilibrium stage. During this stage, the specimen remains into the solution without current enforcement by the galavanostat-potentiostat. The device records the potential and the current density that characterize the specimen into the specific electrolyte. The aim of this stage is the formation of equilibrium on the surface of the specimen.

3.3 Processing the results of CPP

After the completion of the cyclic potentiodynamic polarization test, the software provides a list of the recorded potentials and the respective current densities. The construction of polarization curves requires plotting of potential values versus absolute values of current density. Having these plots, useful conclusions can be drawn by the following analysis.

3.3.1 Tafel extrapolation

One useful clue extracted from the CPP curves is the pitting corrosion current density (i_o). This value is calculated through the Tafel extrapolation method described below. [13], [14]
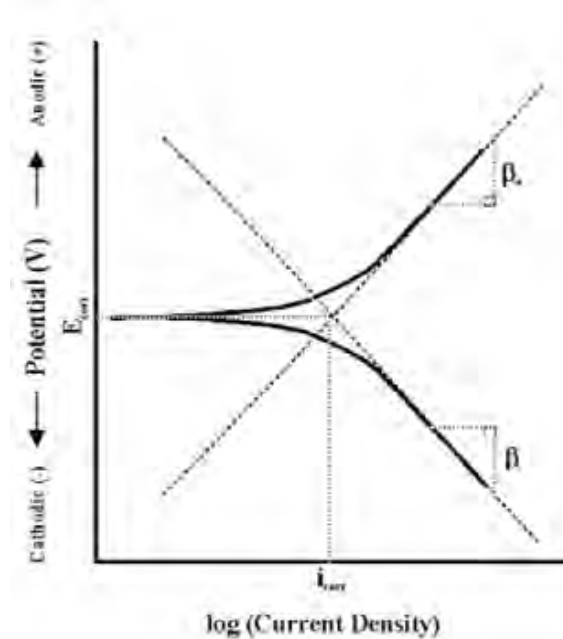
After the completion of the corrosion test, the software provides a list of potentials and the respective current densities. Tafel equation accrues by plotting a diagram with potential values versus current densities in logarithmic scale. In this figure the Tafel equation is extracted by performing the least squares regression method. The linear fit was acceptable only if the regression coefficient was greater than 0,98. It is important to mention that the Tafel region was extended over a current density range of at least one order of magnitude. More analytically, the two Tafel equations are the anodic (3.2) and the cathodic one (3.3). [13], [14]

$$E\text{-}E_{corr} = -\beta\ln(i_{corr}) + \beta\ln i \qquad (3.2)$$

$$E\text{-}E_{corr} = \beta\ln(i_{corr}) - \beta\ln|i| \qquad (3.3)$$

Having identified the pitting corrosion current density, the next step is to calculate the corrosion rate.

3.3.2 Corrosion rate

In case of an alloy the corrosion rate $(r_{corr})_i$ is given by equation (3.4). [15]

$$(r_{corr})_i = K * \left(\frac{i}{d}\right) * EW \qquad (3.4)$$

where : K : conversion coefficient given by Table 3

i : corrosion current density (mA/cm^2)

d : alloy density (g/cm^3) (d_{2707} = 7,8061 g/cm^3)

EW : equivalent weight of the alloy

Table 3 : Values of conversion coefficient K, depending on the preferred corrosion rate units. [15]

Corrosion rate	Current density units	Density units	Values of constant K	Constant K units
mpy	$\mu A/cm^2$	g/cm^3	0,1288	mpy g/(μA cm)
mm/y	A/m^2	Kg/cm^3	327,2	mm Kg/(A m y)
mm/y	$\mu A/cm^2$	g/cm^3	$3,27 * 10^{-3}$	mm g/(μA cm y)

The equivalent weight can be calculated by the equation (3.5).

$$EW = \frac{1}{\sum\frac{ni \cdot fi}{Mi}} \qquad (3.5)$$

where : n_i : degree of ionization of i alloying element

f_i : weight percentage of i alloying element

M_i : atomic weight of i alloying element

Equation (3.5) takes into consideration alloying elements with content in the alloy greater than 1% wt.

 Based on the chemical composition of 2707 from Table 2 the alloying elements that are taken into consideration are given in Table 4:

Table 4 : Elements' info for the calculation of EW.

Alloying element	Degree of ionization (n)	Weight percentage (%)	Atomic weight (g/mol)
Fe	+2	58,225	55,845

Mn	+2	1,5	54,938
Cr	+3	27	51,9961
Ni	+2	6,5	58,6934
Mo	+4	4,8	95,94
Co	+2	1	58,933

According to equation (3.5) and Table 3 the equivalent weight of 2707 is 24,07.

For the characterization of the corroded specimens full metallographic analysis was conducted.

3.4 Stereoscopy

The corroded surfaces were initially examined by using a stereoscope in order to define the severity of pitting corrosion on macroscale level. A Leica Wilz M3Z was employed for this purpose.

3.5 Optical microscopy

The corroded surfaces and respective transverse cross-sections were examined in an optical metallographic microscope in order to acquire further information about the mechanism of corrosion. For this purpose Leitz "Aristomet" was used, at magnifications 50x-500x. In order to reveal the microstructure, electrolytic etching was performed with 10% oxalic acid according to ASTM A262.

3.6 SEM/EDX Analysis

The specimens were further examined by energy-dispersive X-ray spectroscopy (EDX). Line scans and local chemical analysis contributed to the identification of the corrosion mechanism.

3.7 ICP Analysis

The NaCl solution collected from the polarization tests was further analyzed by the inductively coupled plasma (ICP) atomic emission spectroscopy method.

3.8 XPS Analysis

XPS analyses were performed on a Kratos AXIS UltraDLD system, with Aluminium monochromatic X-Ray source (λKa = 1,4866 Å), under high vacuum conditions (10^{-8} torr). The spectra in all of the cases were calibrated by the standard method and were fixed according to the C *1s* peak at 284.6 ±0.2 eV of binding energy (B.E.). Wide-scan spectra (full range) were recorded by 160 eV of passing energy, while High-Resolution (HR) regions by pass energy 20 eV during a three-sweep scan. Shirley (non-linear) baseline was used to subtract the background from the HR peaks and the experimental curves were fitted by a combination of Gaussian (70%) and Lorentzian (30%) distributions}. The sample was studied on a clear surface and on a region with spots.

Chapter 4 : Experimental Results

4.1 Cyclic Potentiodynamic Polarization curves

CPP tests were conducted on the hollow and convex side of the specimens. Figures depict selected polarization curves for reasons of comparison. The comparison is made between two curves for each side separately and also among all the curves. Table 4 sums up the results cyclic potentiodynamic polarization of 2707 in 3,5% wt NaCl solution, in potential range from -1500 mV to +1500 mV as far as the open circuit potential E_{rest}. The results are provided in Figs. 19-21. Test 1 and 8 correspond to convex surface specimen, while test 3 and 7 correspond to hollow surface specimen.

Table 5 : Electrochemical values of the alloys immersed in 3,5% wt. NaCl, at 25 oC. Ecorr : corrosion potential ; Ea/c tr : anodic-to-cathodic transition potential ; Ecp : critical "passivation" potential ; Eb : breakdown potential.

Test	E_{corr} (mV vs. Ag/AgCl)	$E_{a/c\,tr}$ (mV vs. Ag/AgCl)	E_b (mV vs. Ag/AgCl)	E_{cp} (mV vs. Ag/AgCl)	$E_{a/c\,tr}$ - E_{corr} (mV)	E_{cp} - E_{corr} (mV)	E_b - E_{cp} (mV)	E_b - E_{corr} (mV)
1	-218,9	752,02	883,07	-60	970,92	158,9	943,07	1101,97
8	-204,53	612,76	916,22	-60	817,29	144,53	976,22	1120,75
3	-166,19	761,51	962,04	-60	927,7	106,19	1022,04	1128,23
7	-221,67	761,63	962,04	-60	983,3	161,67	1022,04	1183,71

Table 6 : Data extracted from Tafel extrapolation on the polarization curves of hyper-duplex stainless steel 2707 : icorr : corrosion current density ; βc : the Tafel slope ; αc : constant in Tafel equation ; rc2 : regression coefficient of the linear fit ; ΔE : overpotential range for the linear fit ; Δi : current density range for the linear fit ; i_p : current density in the middle of current limiting stage.

Test	i_{corr} (mA/cm²)	β_c (mV/decade)	α_c (mV)	r_c^2	ΔE (mV vs. Ag/AgCl)	Δi (mA/cm²)	i_p (mA/cm²)
1	0,0003	-827,18	-177,53	0,98	(-449,34) – (268,77)	0,0005894 – 0,005877	0,0009034
8	0,000169	-655,26	-119,55	0,99	(-372,49) – (-254,46)	0,000379 – 0,00379	0,0006868
3	0,000045	-644,22	-109,98	0,99	(-326,6) – (-216,2)	0,000112 – 0,00112	0,0004835

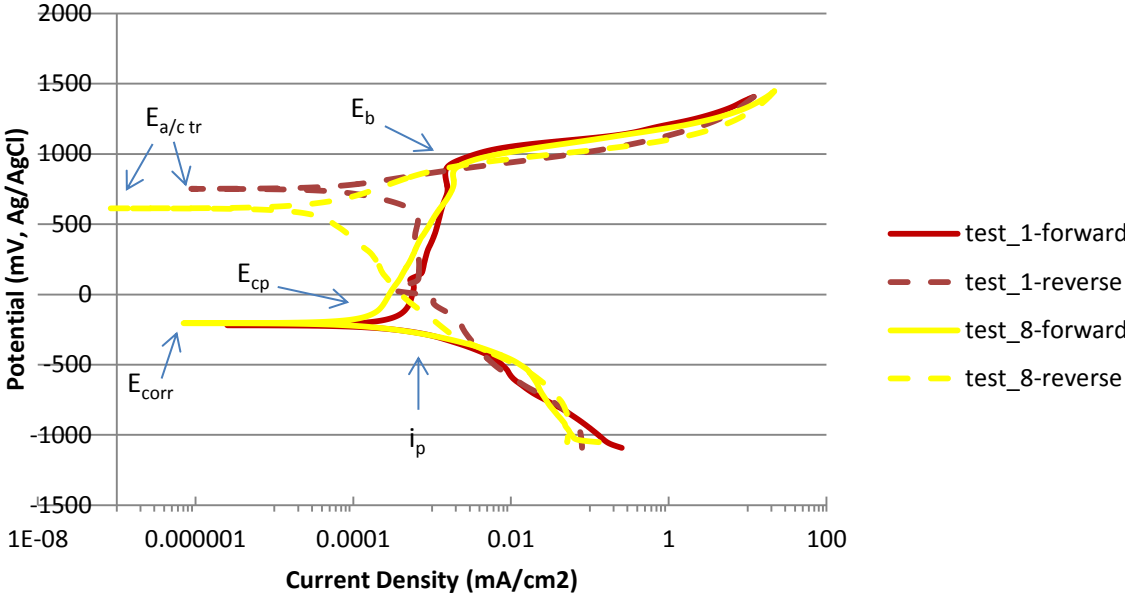| 7	0,000021	-644,05	-90,309	0,99	(-361,37) – (-271,63)	0,0000692 – 0,000694	0,0003336

Figure 19 : Potentiodynamic polarization behavior of outer surface of the specimen.

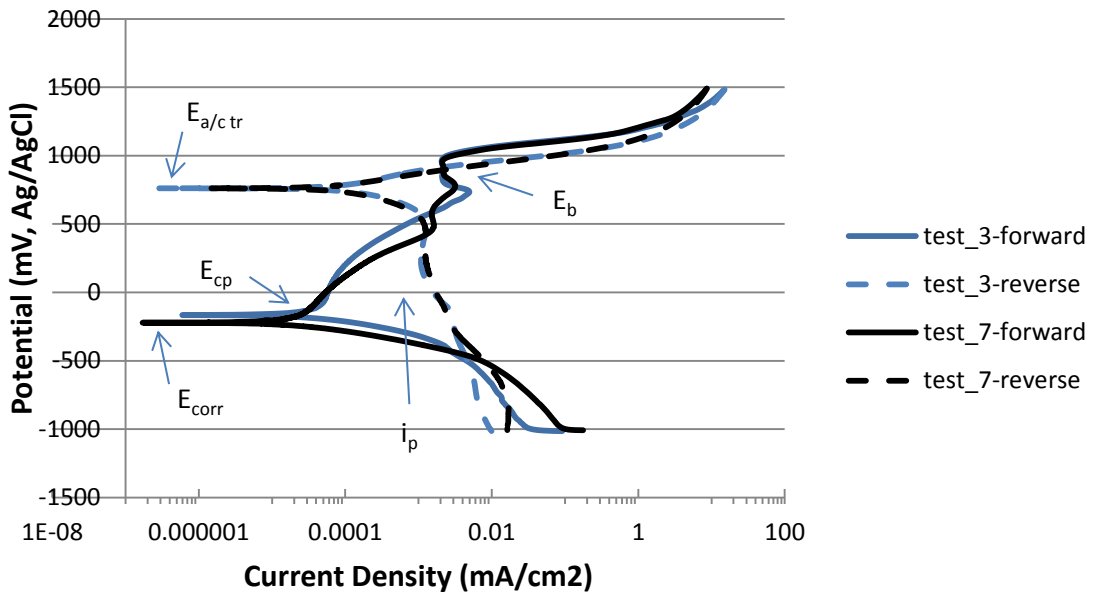# Hyper-Duplex Stainless Steel 2707-3.5% wt NaCl

Figure 20 : Potentiodynamic polarization behavior of inner surface of the specimen.

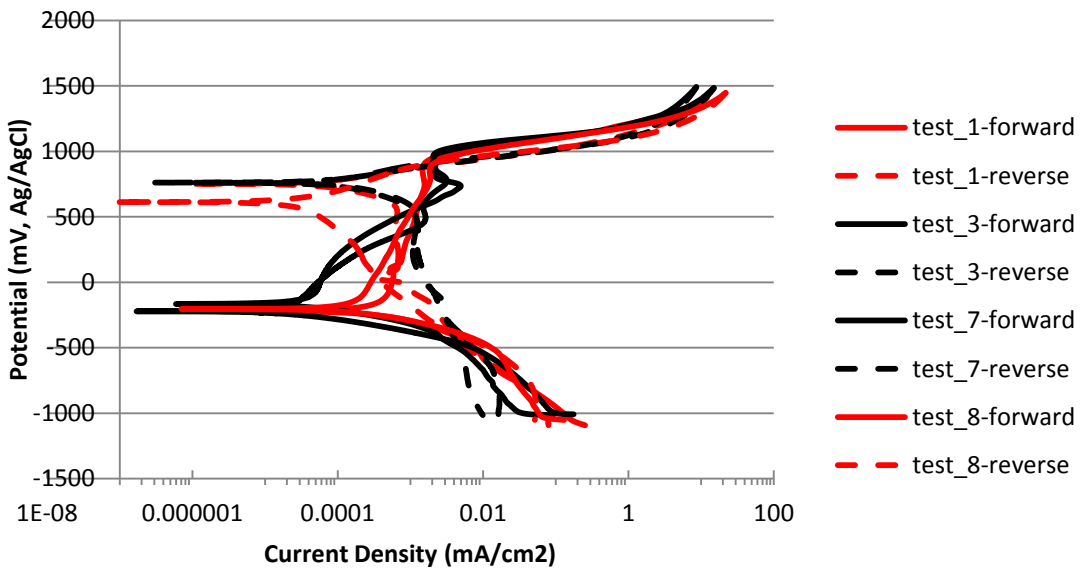# Hyper-Duplex Stainless Steel 2707-3.5% wt NaCl

Figure 21 : Comparison of potentiodynamic polarization behavior between outer and inner surface of the specimen.

In order to draw conclusions from the cyclic potentiodynamic polarization curves, the attention will initially focus on curves from Test 1 and 8 which correspond to examination of curved surface of the specimen.

Test 1 corresponds to the examination of the curved surface of the specimen. At first, during the anodic polarization, an active stage can be distinguished. This stage begins from potential value E_{corr} = -218,9 mV which is the so-called corrosion potential and indicates the transition to the anodic condition. During this active stage, massive increase of the current density is noticed, while the potential changes slightly. Dissolution is considered to happen in this part of the test. At the critical passivation potential E_{cp} the current density decreases sharply, while potential values rise abruptly. In more detail, this stage is defined by the critical passivation potential (E_{cp} = -60 mV) and the breakdown potential (E_b = 883,07 mV). This stage is considered as a stage of real passivation, because i_p<0,1 mA/cm^2 and associated with the formation of surface film. The range of this stage is $\Delta E = E_b - E_{cp}$ = 943,07 mV . The passive regions are usually related with stable corrosion products on the surface of the specimen, which prevent the penetration of the electrolyte. At the breakdown potential (E_b = 883,07 mV) both current density and potential increase at the same time. At this stage a negative hysteresis loop is noticed, but its area, which is set between the forward and the reverse potentiodynamic polarization curve, is quite small. The rapid increase in the current density is attributed to the breakdown of the protective film formed during the stage of passivation. To sum up, at potential values greater than the breakdown potential E_b, dissolution of the passive film occurs. The likelihood of pitting corrosion is not high, as breakdown occurs at E_b more nearly 1000mV higher than E_{cp}. However, the negative hysteresis loop raises the possibility of pitting. SEM and optical microscopy examination will give more information on the extent of pitting. It is important to mention that the pits begin to reclose during the reverse polarization at the potential value E_{rep} = 904 mV, where the surface is repassivates. Hence it is suggested that hyper-duplex SS 2707 has high pitting corrosion resistance in a potential range of E_{rep} = 904 mV to E_{corr} = -218,9 mV. For potential values greater than E_{rep} = 904 mV the severe attack of Cl ions destroys the protective passive film and 2707 is prone to pitting corrosion. This fact indicates a limitation (904mV vs Ag/AgCl) for applications of this duplex SS in artificial seawater (3,5% NaCl solution). One last notice accrues from the comparison between E_{corr} = -218,9 mV and the corrosion reverse potential $E_{a/c\ tr}$ = 752,02 mV. The superiority of the reverse corrosion potential is accompanied by nobler corrosion products, formed in the reverse polarization, in comparison with those formed during forward polarization.

Identical behavior is noticed in Test 8. In this case, a negative hysteresis loop also appears, covering almost the same area as in Test 1. Breakdown potential seems

to be of the same size. The only differences between these two tests are the less noble corrosion reverse potential $E_{a/c\ tr}$ = 612,76 mV compared to E_{corr} = -204,53 mV and, also, the earlier passivation potential, which corresponds to lower current density.

As far as Test 3 and 7 the anodic polarization curves do not represent a typical active-passive behavior. These tests correspond to the hollow surface of the specimen. Both curves include regions with slight reduction of the rate of current increase or regions of current decrease and subsequent persistent increase in the current density values. This complex form can be divided in five stages. In Test 7 during stage 1, active corrosion takes place starting for corrosion potential E_{corr} = 221,67mV until a slight decrease in the rate of current density increase (stage 2). Stage 2 is limited by a stage of remarkable increase in current density, over one order of magnitude (stage 3). This sharp increase is succeeded by a passivation stage, which extends in a potential range from 477 mV to 960 mV (stage 4). This passive stage can be divided in two sub-stages of passivation with the first one ending at a potential value of 620 mV and the second one starting at 790 mV. The intermediate part is characterized by simultaneous increase of potential and current density with the same rate. Finally, an abrupt increase in density is noticed (stage 5).

Regarding the reverse polarization, the small area covered by the negative hysteresis loop indicates a satisfactory susceptibility to pitting corrosion. Also, the anodic-to-cathodic transition potential $E_{a/c\ tr}$ = 761,63 mV is by far nobler than the corrosion potential E_{corr} = 221,67 mV, which implies nobler surfaces. Reverse polarization curve intersects the forward one at a potential value of 895 mV. This value sets an upper limit (895 mV) for the application of 2707 in a chloride containing environment.

As far as Test 3, a similar behavior is noticed. Stage 1 and 2 follow the same route, with unique exception the corrosion potential value, which proves to be nobler (E_{corr} = -166,19 mV) than the respective value in Test 7. Stage 3 expands in a wider range of current density, while the passivation stage (stage 4) occupies a slight range of potential, from 820 mV to 960 mV. At last, the area of the negative hysteresis loop and the anodic-to-cathodic potential are identical with those in Test 7.

Figure allows an aggregated comparison of all polarization curves. The conclusions drawn from these curves are summarized below :

- Corrosion potential E_{corr} remains identical in every polarization test.
- Anodic-to-cathodic transition potential takes similar values in all curves and are always nobler than the corrosion potential E_{corr}.

- Negative hysteresis loop appears in all occasions, with comparable area covered.
- In the case of the convex surface of the specimen, current stabilization takes place at E_{cp}. However, in the case of the hollow surface specimen, current stabilization takes place at much higher potential, although drastic current decrease has started at an E_{cp} comparable to the E_{cp} of the convex surface specimen curves. This phenomenon will be explained subsequently.

In general, the corrosion current density i_{corr} and the corrosion potential E_{corr} are used in order to determine the susceptibility of the specimen to active dissolution, while the passivation current density i_p and the passivation potential E_p are used to define the passivation ability of the specimen. Furthermore, the passivation current density and the range of the passivation area indicate the stability of the formed passive films.

- The corrosion rate can be calculated according to equation (3.4). The sequence of the corrosion rates of the four specimens is :
- The corrosion current densities follow the sequence :

$i_{corr,test\ 7}$=0,000021 mA/cm^2 < $i_{corr,test\ 3}$=0,000045 mA/cm^2 < $i_{corr,test\ 8}$=0,000169 mA/cm^2 < $i_{corr,test\ 1}$=0,0003 mA/cm^2.

- The passivation current densities are classified as such :

$i_{p,test\ 7}$=0,0003336 mA/cm^2 < $i_{p,test\ 3}$=0,0004835 mA/cm^2 < $i_{p,test\ 8}$=0,0006868 mA/cm^2 < $i_{p,test\ 1}$=0,0009034 mA/cm^2.

- As far as the difference between critical passivation potential E_{cp} and corrosion potential E_{corr} , its size represents the ability for passivation. Starting with the greater ability the sequence is :

E_{cp}-$E_{corr\ (test\ 3)}$ = 106,19 mV < E_{cp}-$E_{corr\ (test\ 8)}$ = 144,53 mV < E_{cp}-$E_{corr\ (test\ 1)}$ =158,9 mV < E_{cp}-$E_{corr\ (test\ 7)}$ = 161,67 mV.

- The comparison of the difference between the breakdown potential E_b and the corrosion potential E_{corr} is shown by the following sequence, starting from the specimen with the weakest corrosion resistance :

$E_b - E_{corr\ (test1)}$ = 1101,97 mV < $E_b - E_{corr\ (test8)}$ = 1120,75 mV < $E_b - E_{corr\ (test3)}$ = 1128,23 mV < $E_b - E_{corr\ (test7)}$ = 1183,71 mV.

- Regarding the range of the passive region the sequence is :

$E_b - E_{cp\ (test1)}$ = 943,07 mV < $E_b - E_{cp\ (test8)}$ = 976,22 mV < $E_b - E_{cp\ (test3)}$ = $E_b - E_{cp\ (test8)}$ = 1022,04 mV.

4.1.1 Corrosion Rate

One main advantage of the cyclic potentiodynamic polarization curves, besides the prediction of the material's behavior in corrosive environments, is the calculation of the corrosion current density. Through this value the corrosion rate can be defined. With the aid of equation (3.4) the corrosion rate can be calculated. (Table 7) It is noticed that the corrosion rate is particularly low.

Table 7 : Corrosion rate.

Test	Corrosion Rate	
	mpy	mm/y
1	0,00012	0,000003
8	0,00007	0,000002
3	0,00002	0,0000004
7	0,00001	0,0000002

The above values of corrosion rate are smaller, by approximately 4 orders of magnitude, than corrosion rates that indicate a significant corrosion resistance of alloys with high cost. For these alloys, corrosion rate <75 μm/y indicates high resistance to uniform corrosion. [14]

4.2 Optical Microscopy

The microstructure of the as-received steel is shown in Fig.22. It consists of ferrite and austenite. The white area corresponds to ferritic phase, while the darker to austenitic.
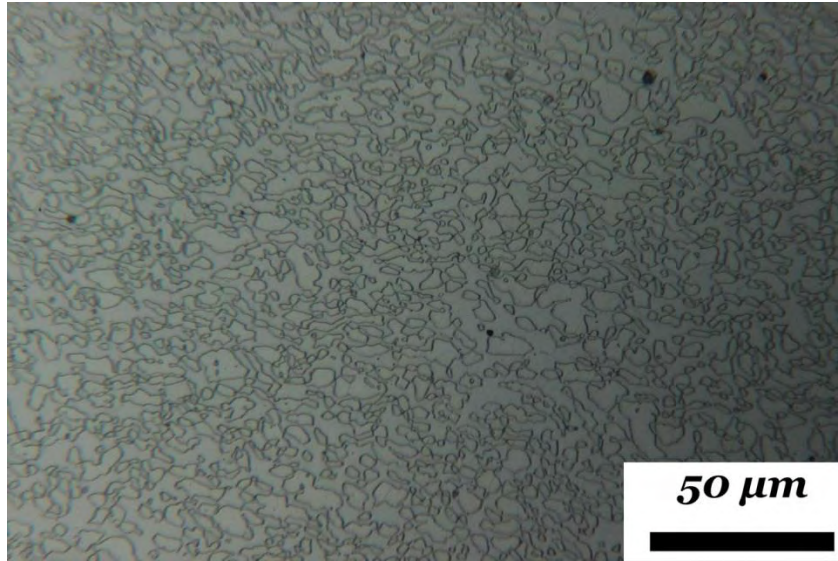
Figure 22 : Microstructure in transverse cross section area of 2707.

The microstructure at the exposed surface is presented in Figs. 23 and 24. This microstructure corresponds to the cross section area of the specimen and focuses on the area with pits. It is obvious from Fig. 24 that the white area has been "consumed" compared to Figure 22. This fact provides crucial information for the mechanism of corrosion. As the white area depicts the ferritic phase, it is concluded that ferrite seems to be more prone to pitting corrosion.
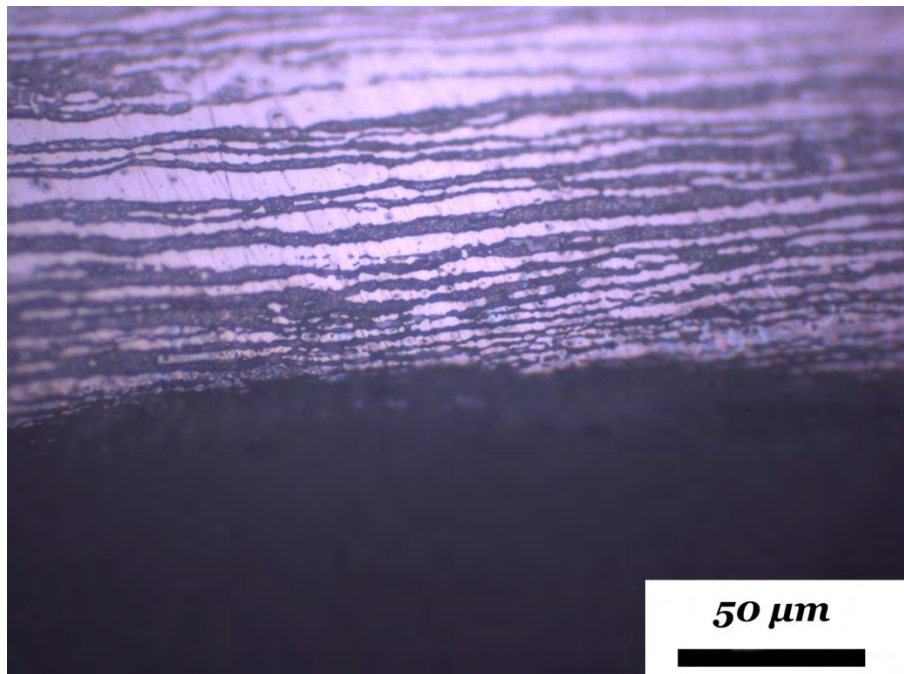

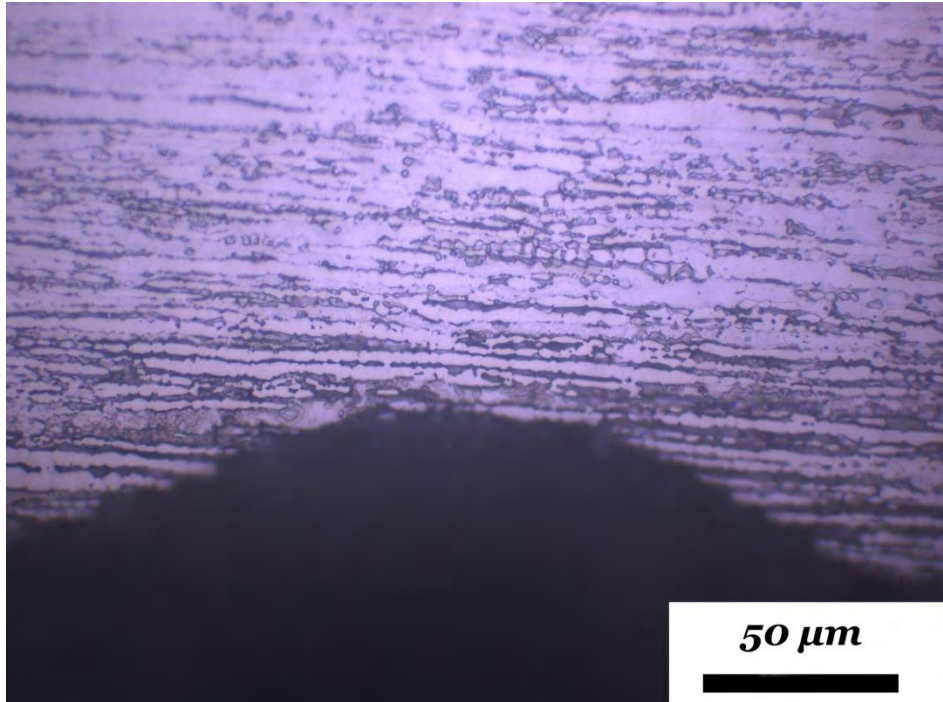**Figure 23 : Microstructure at the area of a pit.**

Figure 24 : Microstructure at the area of a deeper pit.

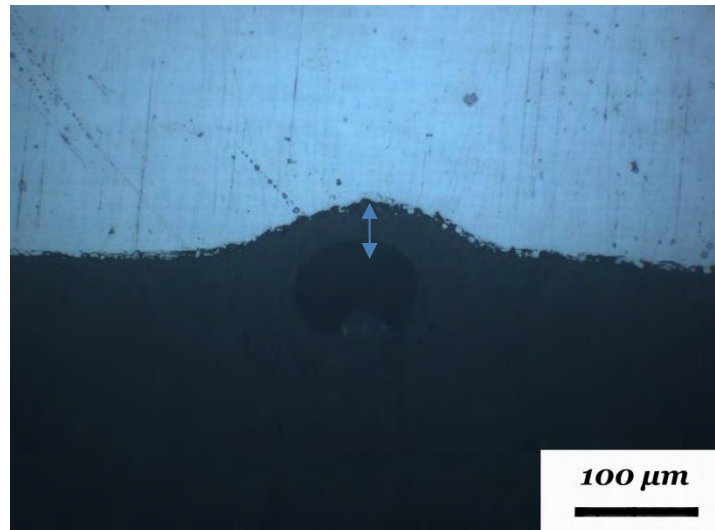As regards the depth of the pits, the pit that seemed more severe was examined (Fig. 25).

Figure 25 : Depth of the most severe pit.

Based on the scale, the depth of this pit is 38 μm.

4.3 Results of SEM/EDX Analysis

Each corroded specimen was examined by SEM/EDX in order to gather further details about the corrosion mechanism that occurred during the cyclic potentiodynamic polarization tests.

4.3.1 Surface examination

In Fig. 26 spot chemical analysis results, acquired from the surface of a typical corroded specimen are provided. It seems that Cl has penetrated inside the pits. In addition, Cr, Mo and Ni appear to have variations in relation to the inner and the outer area of the pits, as clearly demonstrated by the line scans shown in Figs. 27, 28 and 29. Concentrations are measure in wt. %.

According to the results of the line scans, compositions in weight of Fe and Cr seem to be reduced inside the pits. The reduction of Cr accrues the dissolution of the protective passive oxide film Cr-O. Therefore, the alloy was left unprotected in spots where pits were formed on the surface. As regards the composition of Mo, a slight reduction is noticed inside the pits.
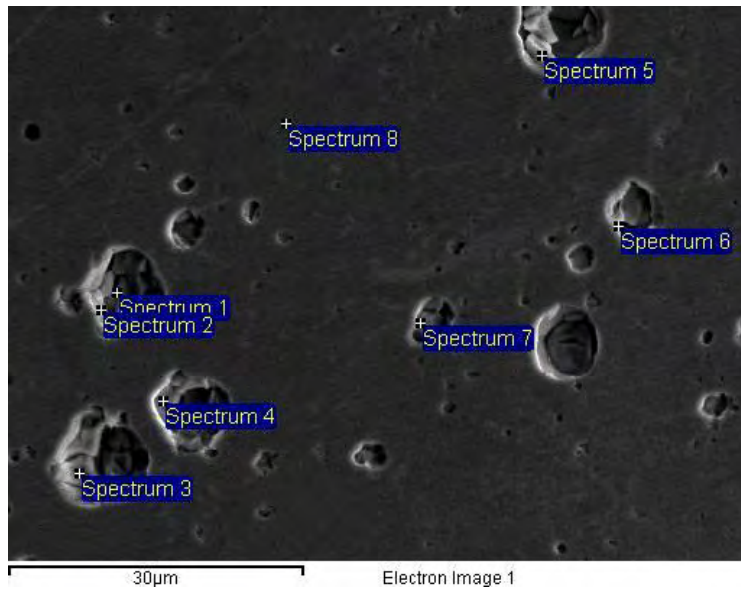
Spectrum	In stats.	O	Na	Si	Cl	Cr	Fe	Ni	Mo	Total
Spectrum 1	Yes	0.34	0.80	0.09	0.64	38.19	55.80	3.52	0.62	100.00
Spectrum 2	Yes	2.71	6.50	0.54	2.38	24.31	50.86	7.58	5.10	100.00
Spectrum 3	Yes	3.27	0.15	0.23	-0.02	27.20	57.70	6.98	4.48	100.00
Spectrum 4	Yes	2.66	1.35	0.39	0.34	25.05	56.94	5.83	7.43	100.00
Spectrum 5	Yes	2.13	0.22	1.06	-0.07	27.16	58.65	7.80	3.04	100.00
Spectrum 6	Yes	1.11	5.38	0.19	2.72	27.18	54.70	3.97	4.76	100.00
Spectrum 7	Yes	2.10	0.03	-0.03	0.00	29.18	56.73	5.79	6.19	100.00
Spectrum 8	Yes	1.96	0.61	0.29	0.36	29.06	56.13	4.29	7.31	100.00

Figure 26 : Spot chemical analysis at the surface of the corroded specimen
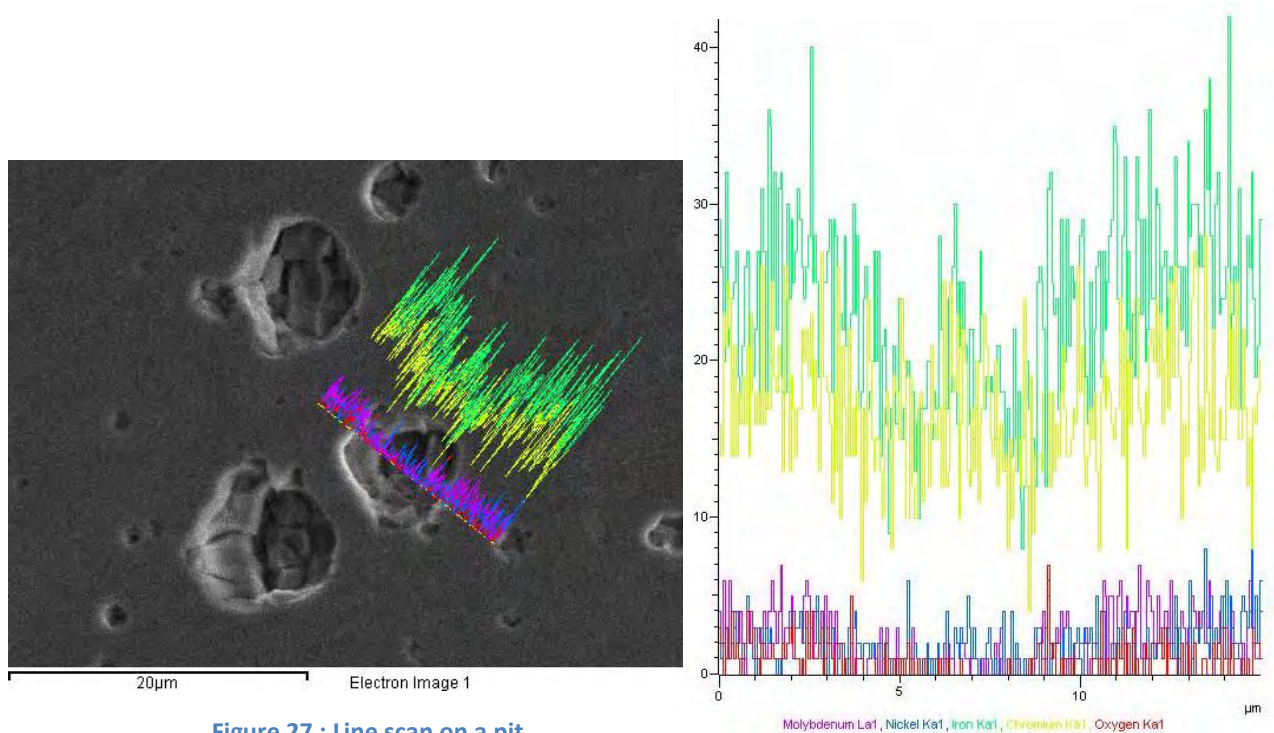

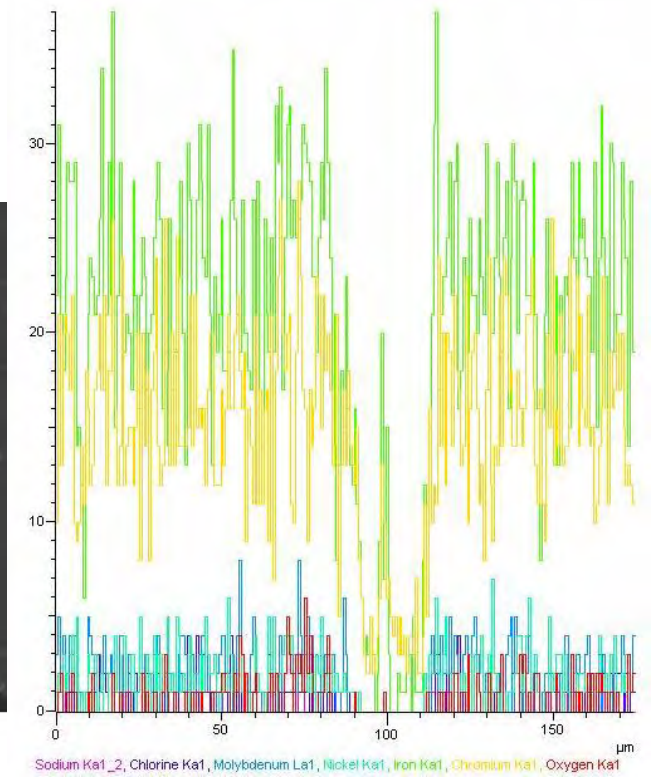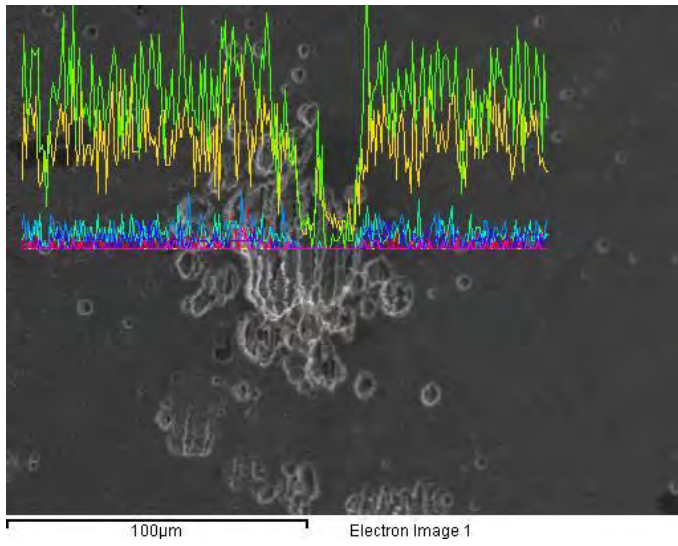
Figure 27 : Line scan on a pit.

35

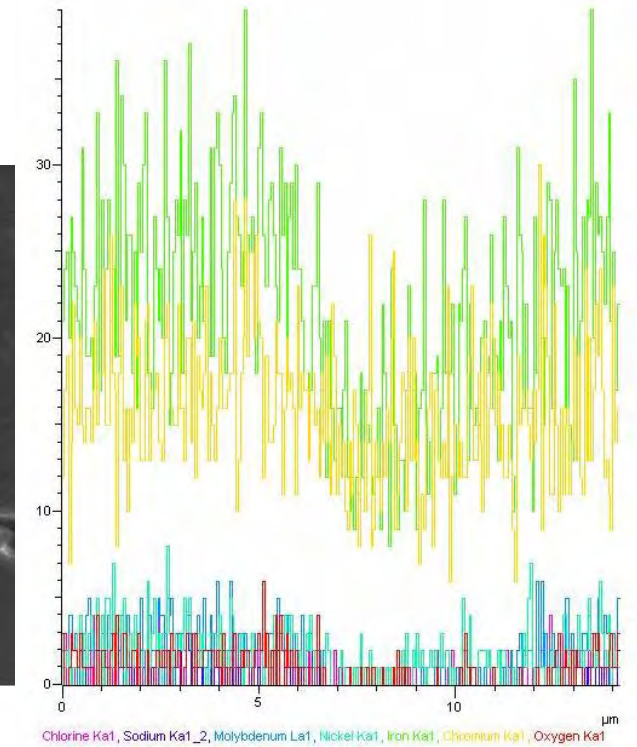**Figure 28 : Line scan on an array of pits.**
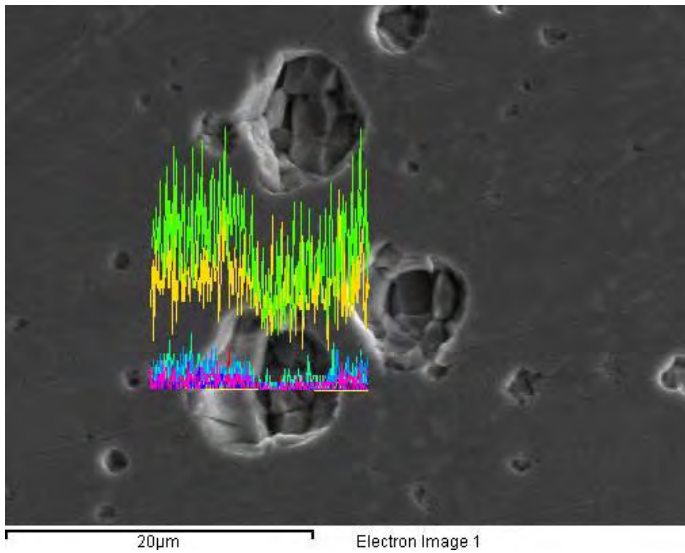
Figure 29 : Line scan on a pit.

4.3.2 Cross-section examination

In Figs. 30, 31 and 32 spot chemical analysis results, acquired from the transverse cross-section of a typical corroded specimen are provided. Concentrations are measure in wt. %.

It is obvious that a general reduction of composition of Cr and Ni has occurred inside the pit.

It is remarkable that in each spectrum, concentration of these two elements (Cr & Ni) is by far below the respective percentages in the initial composition of the alloy.

Furthermore, line scans inside the pitting provide more information about the mechanism of corrosion (Figs. 33 and 34). It is shown that lack of chromium (Cr) has left the alloy unprotected against the chlorine ions, as the protective film has been dissolved.

Also, mapping in the area of the transverse cross-section inside the pitting indicates variations in the concentrations of Cr and Ni close to edge of the pitting (Fig 35).
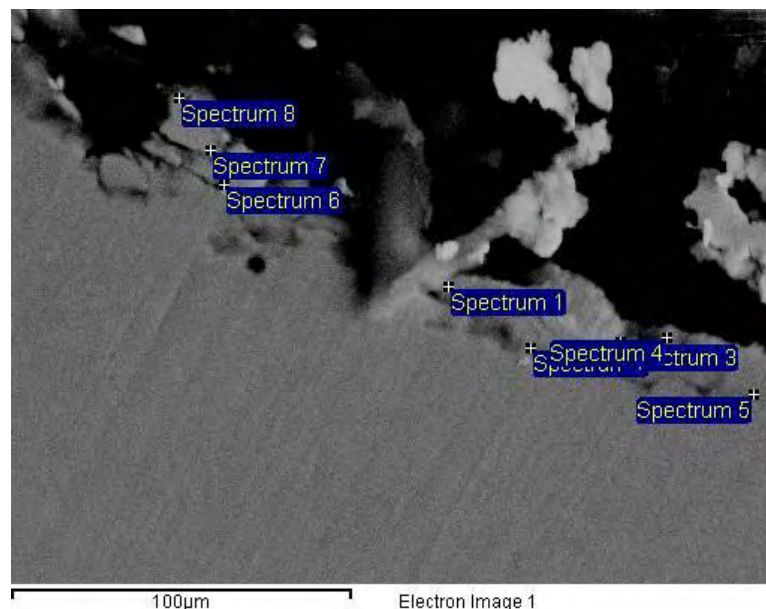
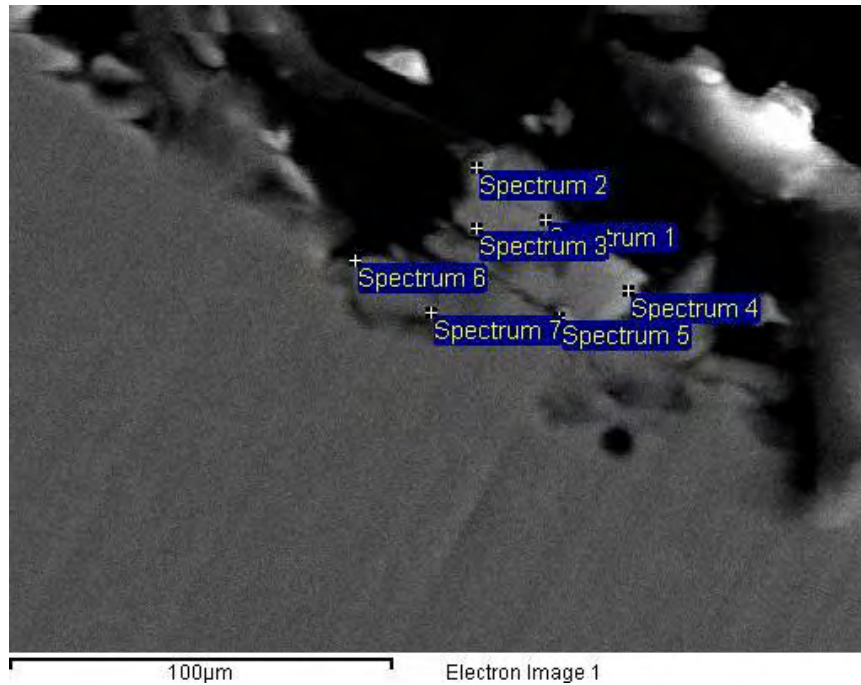| Spectrum	In stats.	O	Si	Cl	Cr	Fe	Ni	Mo	Total
Spectrum 1	Yes	6.23	0.24	0.09	26.10	56.01	4.81	6.52	100.00
Spectrum 2	Yes	2.08	0.42	-0.20	27.86	58.26	4.76	6.83	100.00
Spectrum 3	Yes	6.41	0.77	0.10	27.99	53.20	4.39	7.15	100.00
Spectrum 4	Yes	3.02	0.53	0.17	28.73	57.09	4.82	5.64	100.00
Spectrum 5	Yes	0.92	0.12	0.17	28.60	59.64	4.78	5.77	100.00
Spectrum 6	Yes	4.12	0.75	0.17	27.16	57.15	5.58	5.08	100.00
Spectrum 7	Yes	2.81	0.61	-0.16	26.05	58.35	9.08	3.25	100.00
Spectrum 8	Yes	15.76	0.49	0.06	23.01	49.77	6.17	4.73	100.00
Sum Spectrum	Yes	2.86	0.47	0.22	27.96	56.97	5.48	6.05	100.00

Figure 30 : Spot chemical analysis at the area of a pit in transverse cross-section.

Spectrum	In stats.	O	Si	Cl	Cr	Fe	Ni	Mo	Total
Spectrum 1	Yes	7.67	0.28	0.05	24.74	56.25	6.40	4.61	100.00
Spectrum 2	Yes	13.93	0.81	0.38	23.45	51.61	5.40	4.41	100.00
Spectrum 3	Yes	1.89	0.35	0.15	25.79	59.75	7.67	4.39	100.00
Spectrum 4	Yes	3.70	0.70	0.09	25.64	58.10	7.92	3.85	100.00
Spectrum 5	Yes	1.50	0.83	-0.06	27.81	57.67	4.93	7.32	100.00
Spectrum 6	Yes	12.35	0.88	0.40	26.30	51.41	5.28	3.37	100.00
Spectrum 7	Yes	3.36	0.30	0.45	26.06	57.94	6.28	5.61	100.00
Sum Spectrum	Yes	4.20	0.72	0.14	27.53	56.40	5.50	5.52	100.00

Figure 31 : Spot chemical analysis closer to the pit in transverse cross-section.

39
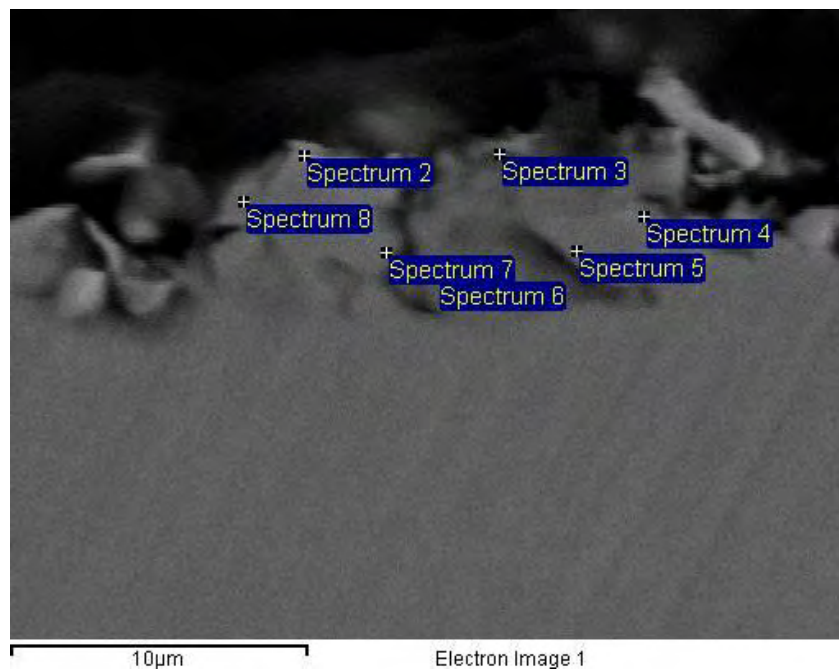
Spectrum	In stats.	O	Si	Cl	Cr	Fe	Ni	Mo	Total
Sum Spectrum	Yes	4.08	0.04	0.17	26.60	57.15	7.57	4.38	100.00
Spectrum 2	Yes	40.59	1.92	1.83	18.31	32.92	4.04	0.40	100.00
Spectrum 3	Yes	32.16	1.45	0.88	21.05	34.77	4.38	5.32	100.00
Spectrum 4	Yes	14.95	1.01	0.79	20.87	49.67	7.41	5.30	100.00
Spectrum 5	Yes	6.50	0.48	-0.10	26.90	54.07	9.11	3.04	100.00
Spectrum 6	Yes	2.59	0.59	0.42	25.27	58.98	8.14	4.02	100.00
Spectrum 7	Yes	5.48	0.68	0.40	24.83	57.81	7.04	3.77	100.00
Spectrum 8	Yes	38.34	0.93	3.18	18.30	33.63	3.25	2.37	100.00

Figure 32 : Spot chemical analysis at the area of the pit with remarkable reduction of chromium (Cr) concentration.
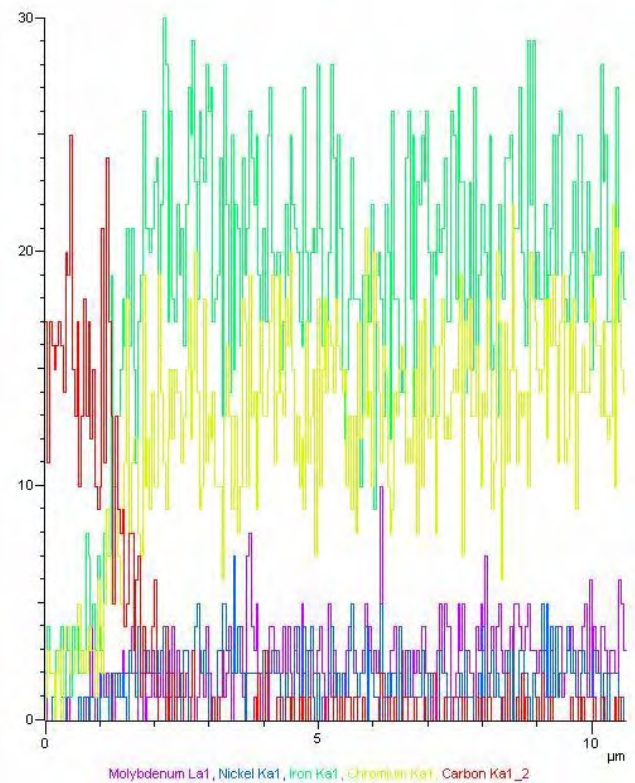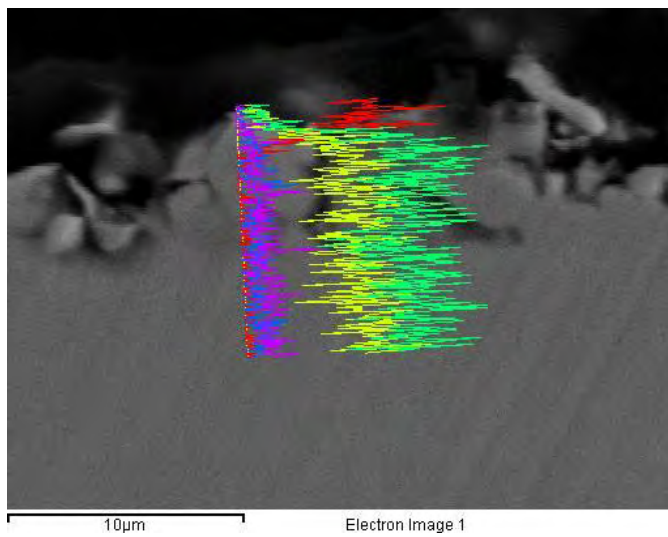

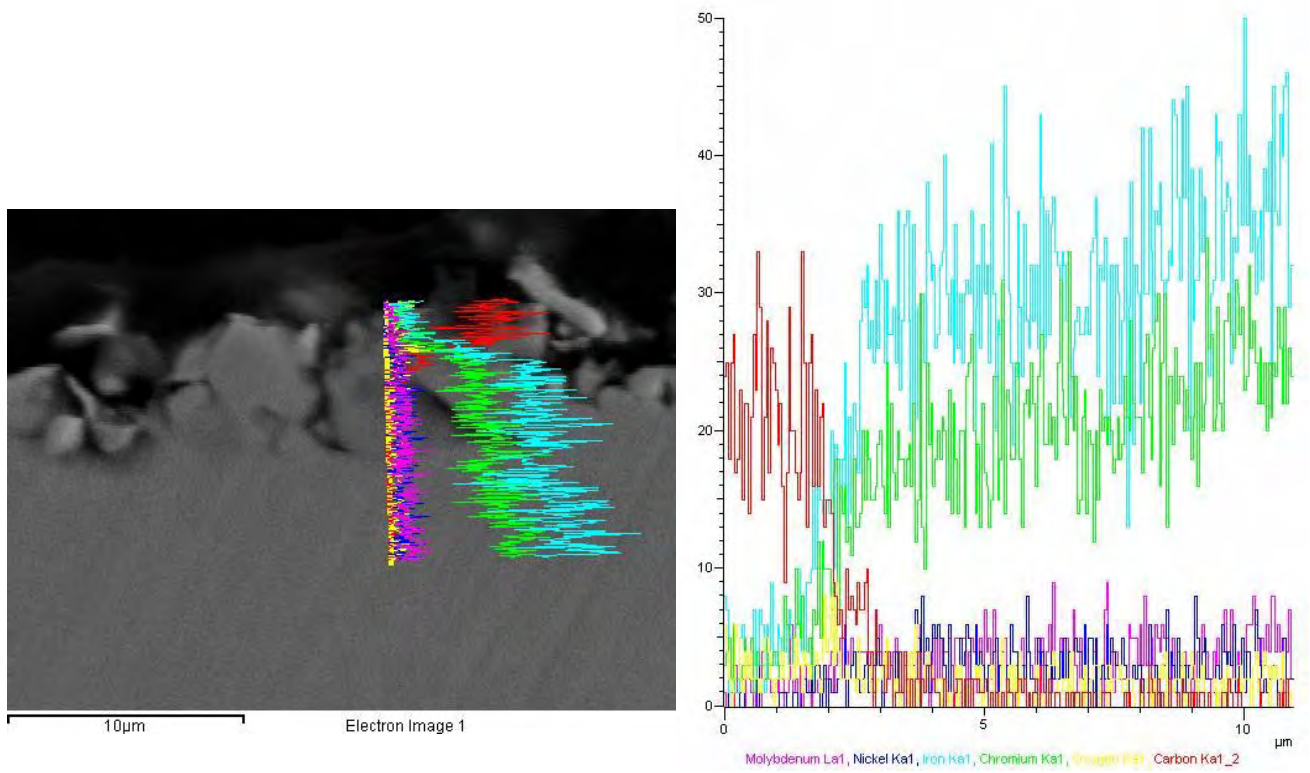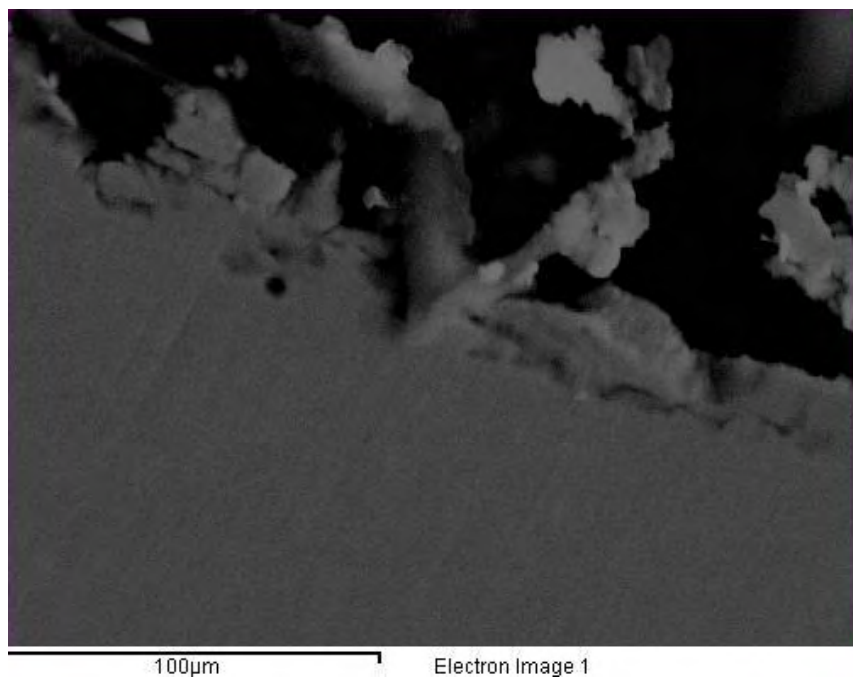**Figure 33 : Line scan at the edge of the pit.**

Figure 34 : Line scan at the edge of the pit.

C Ka1_2

O Ka1

Si Ka1

Cr Ka1

Fe Ka1

Ni Ka1

Mo La1
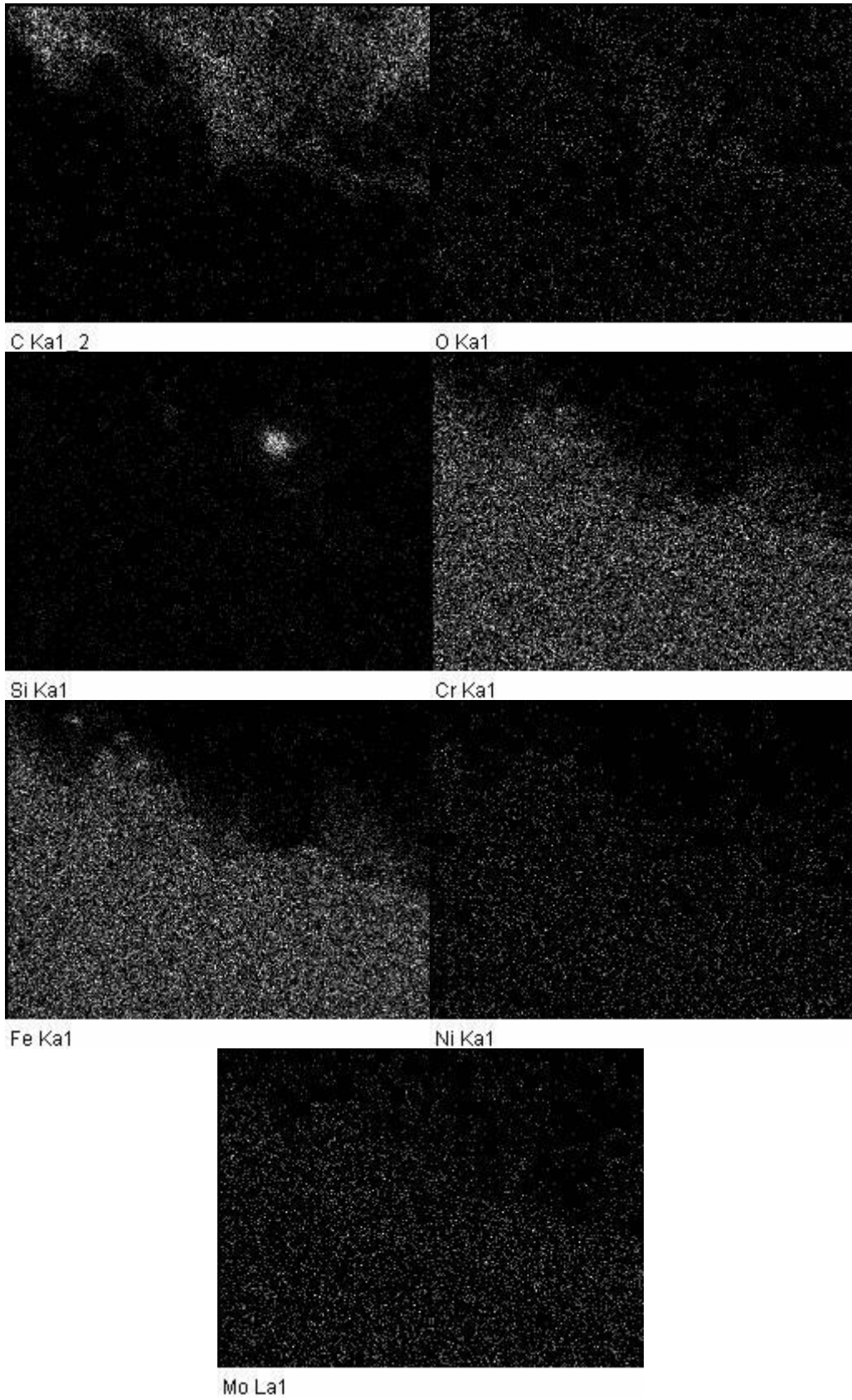
Figure 35 : Mapping close to the pit in transverse cross-section.

4.4 Results of ICP Analysis

ICP analysis was conducted in the NaCl solution after the cyclic potentiodynamic polarization tests. The first analysis corresponds to the outer surface of the specimen, while the second to the inner surface. Results in ppm are shown on the following table. Both measurements confirm some dissolution of the chromium surface film.

Table 8 : Results of ICP Analysis

Solution	Cr	Fe	Ni	Mo
No. 1	1,8	0,4	0,4	0,5
No. 2	2	0,3	0,0	0,0

4.5 Results of XPS Analysis

Wide-scan spectra (Fig. 36) was identical referring to the stoichiometry of the sample analysis positions. The main difference concerns the relative received intensities from the elements, concluding in small differences in presentence atomic concentrations.
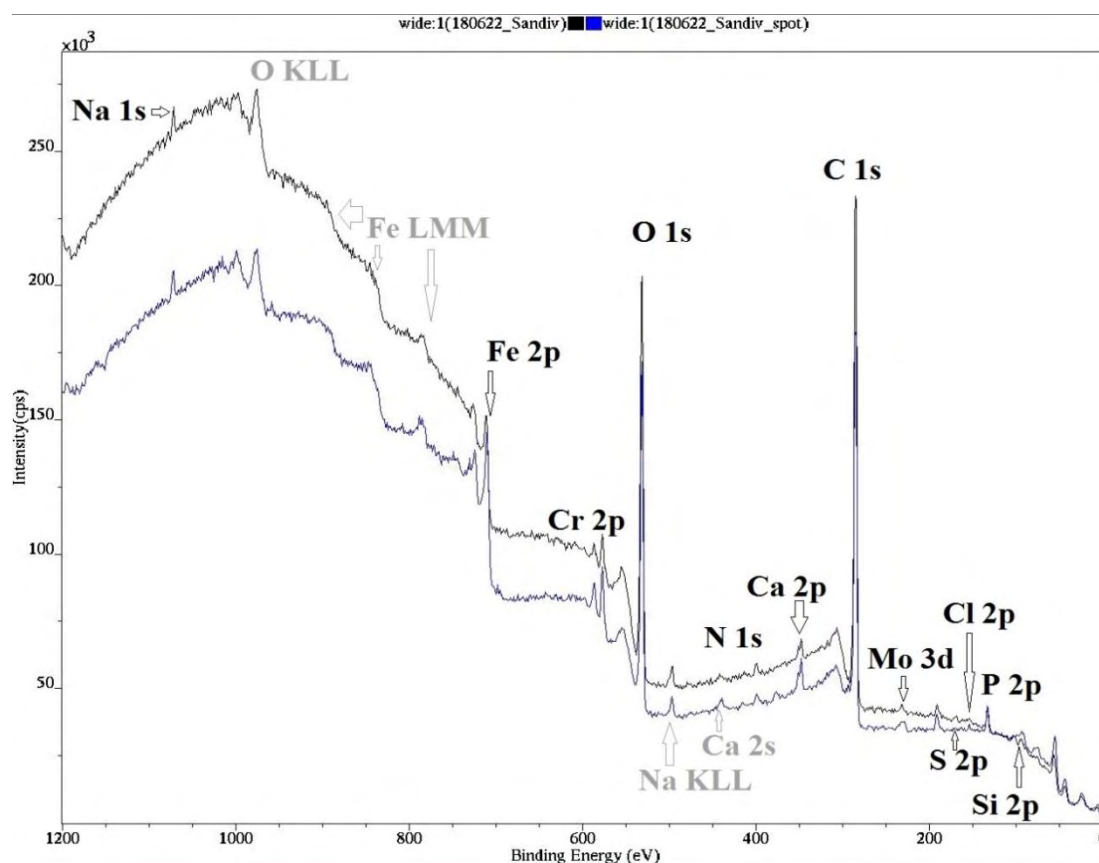
4.5.1 Clear surface

The first conclusion extracted from the deconvolution of the HR peaks from the *1s* orbital of C is the carbon contamination due to expose of the clear surface to the atmosphere. In more detail, the following bonds are formed : C-O, C-O-C and C-O-H, and C=O at 284,6, 286 and 288,5 eV respectively. Furthermore, the *1s* orbitals of O with peaks at 530,7 and 532,2 eV indicate the presence of C-O-H bonds, while the peak at around 529,1 eV corresponds to the binding energy of the metal oxides (mainly ferric oxides [19]).
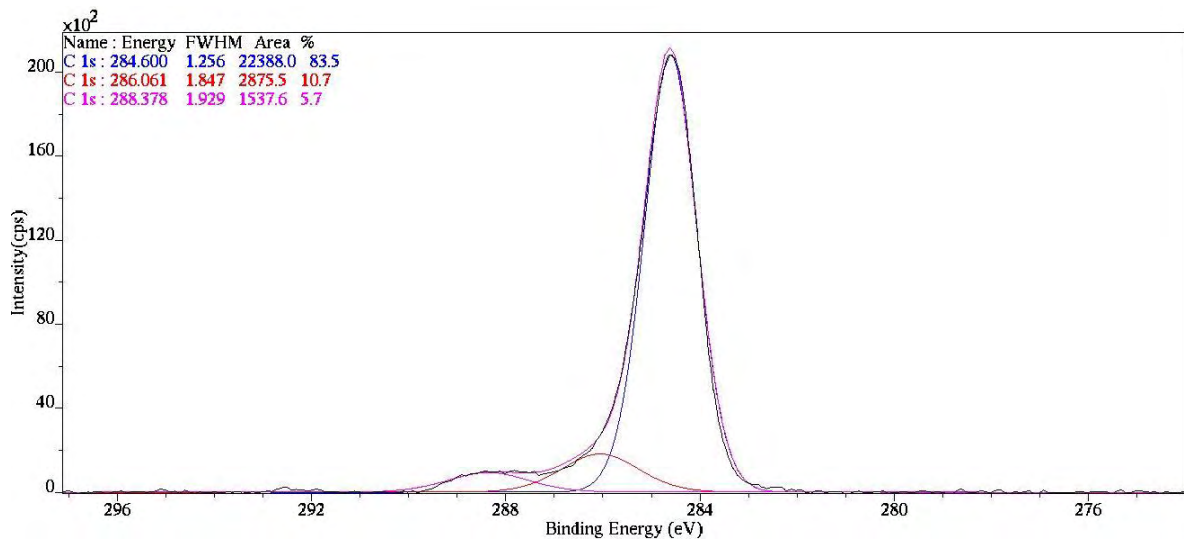
Figure 37 : C-1s HR peak deconvolution
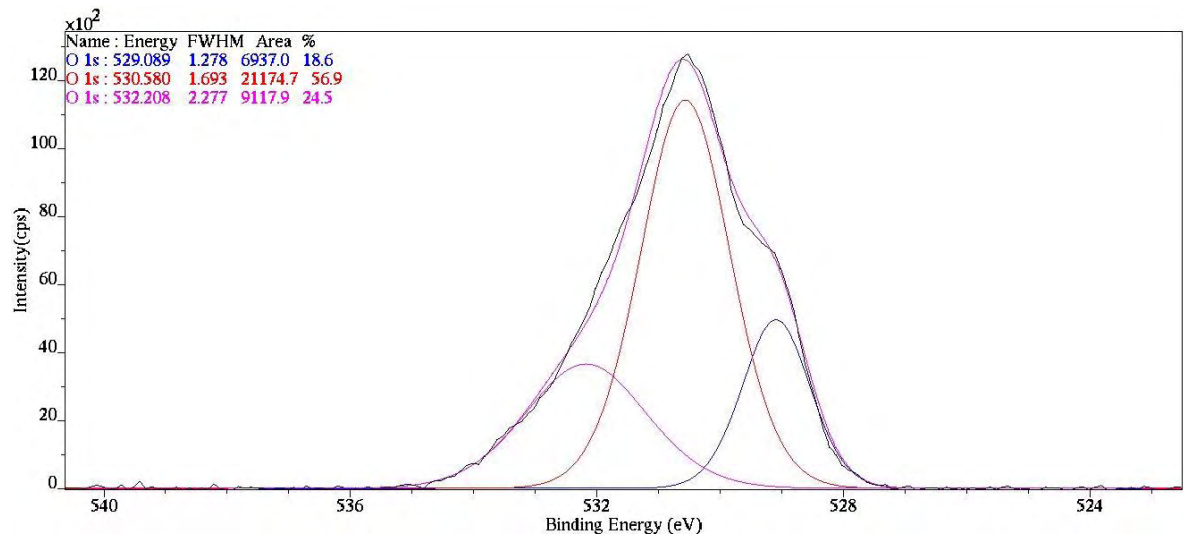
Figure 38 : O-1s HR peak deconvolution

The analysis of the Fe *-2p* peaks, revealed that the surface metal is completely oxidized, having two different oxidized states. The Fe^{+2} and Fe^{+3}. The Fe *-2p$_{3/2}$* orbital's peak position at 709.6eV originated from the divalent iron, while the one at 711.8 for the trivalent, to form Fe_2O_3 and/or Fe_3O_4, FeO [20], [21] and possibly FeOOH [22].
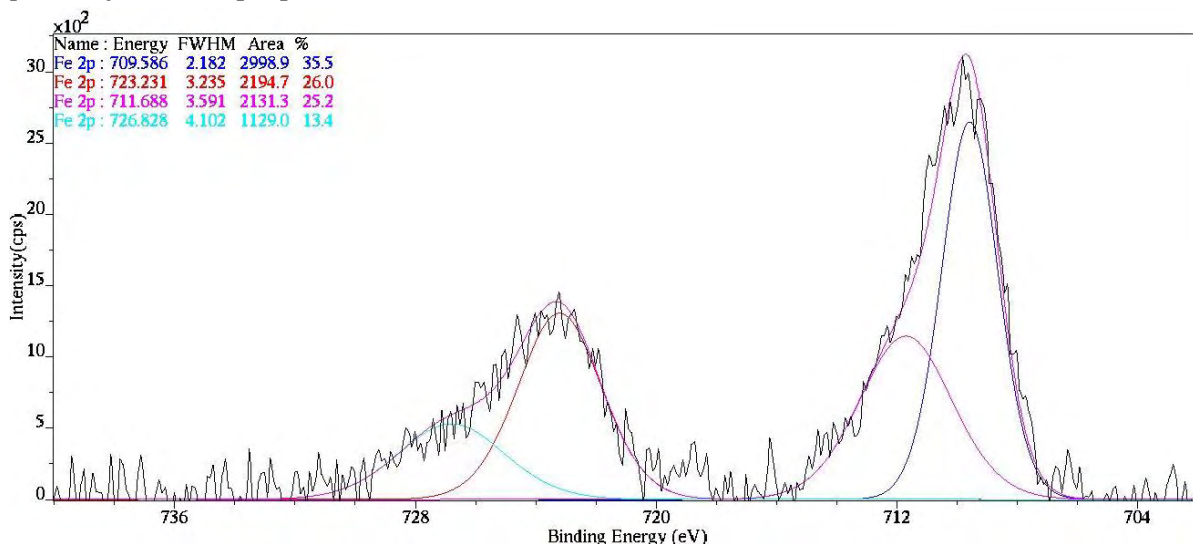
Figure 39 : Fe-1s HR peak deconvolution

Cr appears oxidized (*2p$_{3/2}$* peak at 575.8eV for the Cr_2O_3 [20], [23]), but there is a small contribution from metallic Cr (-2p$_{3/2}$ peak for Cr^0 at 573.1eV [24], [25]) too. The oxidized/metallic ratio was calculated at about 23:2.
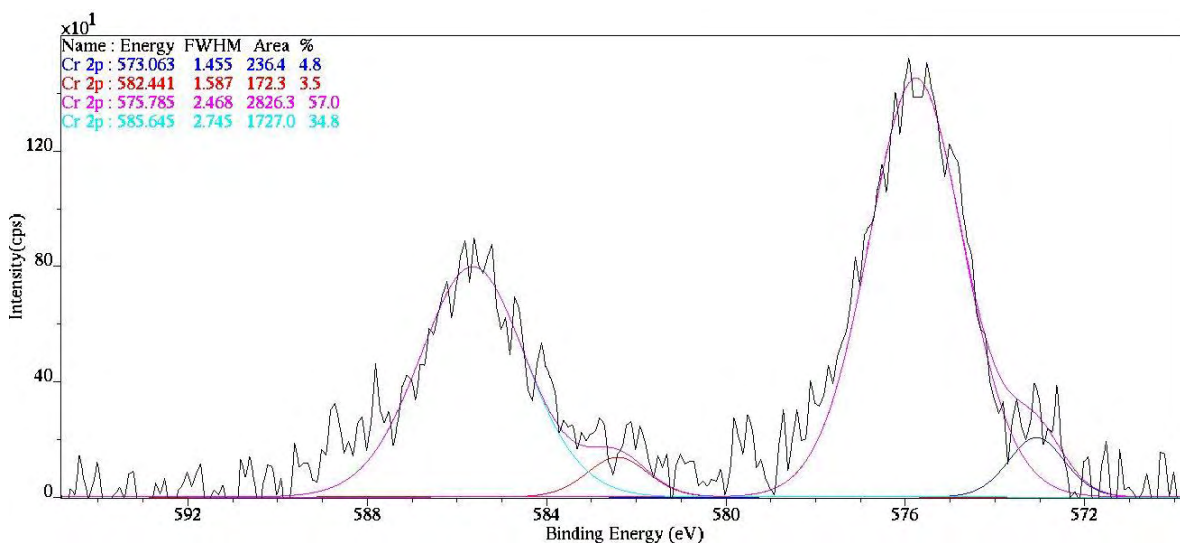
Figure 40 : Cr-1s HR peak deconvolution

Concerning P 2p high resolution peaks (*2p3/2* at 132.3eV) , the results conclude the PO$_4$ state of the element, with metallic bonds to form Fe(PO$_4$) [26], [27]. The relative O *-1s* peak at 530.2eV was not able to be depicted in Fig. 38, due to the dominant contribution from the carbon oxides (P in low concentrations comparatively to the surface C).
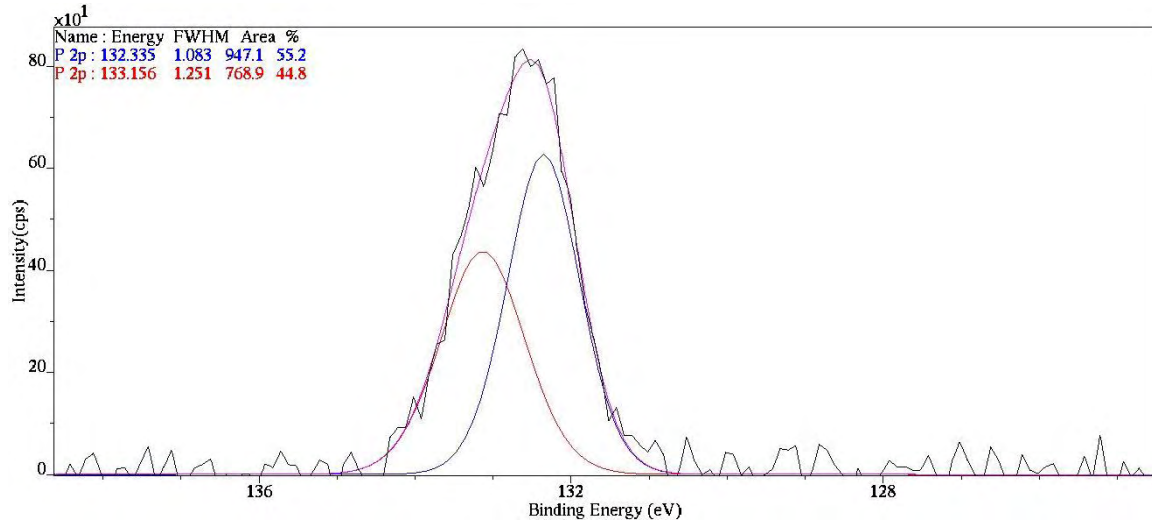
Figure 41 : P-1s HR peak deconvolution

The deconvolution of Na *-1s* peak from the clear surface, provided the typical peak at 1070.7eV for the Na$^+$ [28–30]. Usually it referred to the hydrated calcium or/and to the NaCl compound.
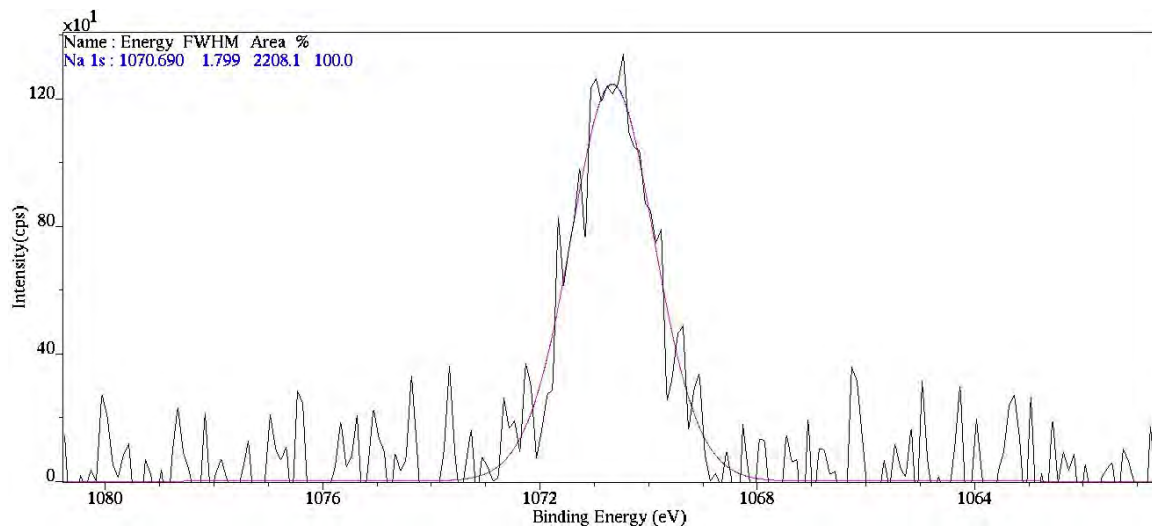
Figure 42 : Na-1s HR peak deconvolution

Finally, N *-1s* peak at 339.3eV is characteristic for the the N-C bonds [31–33].
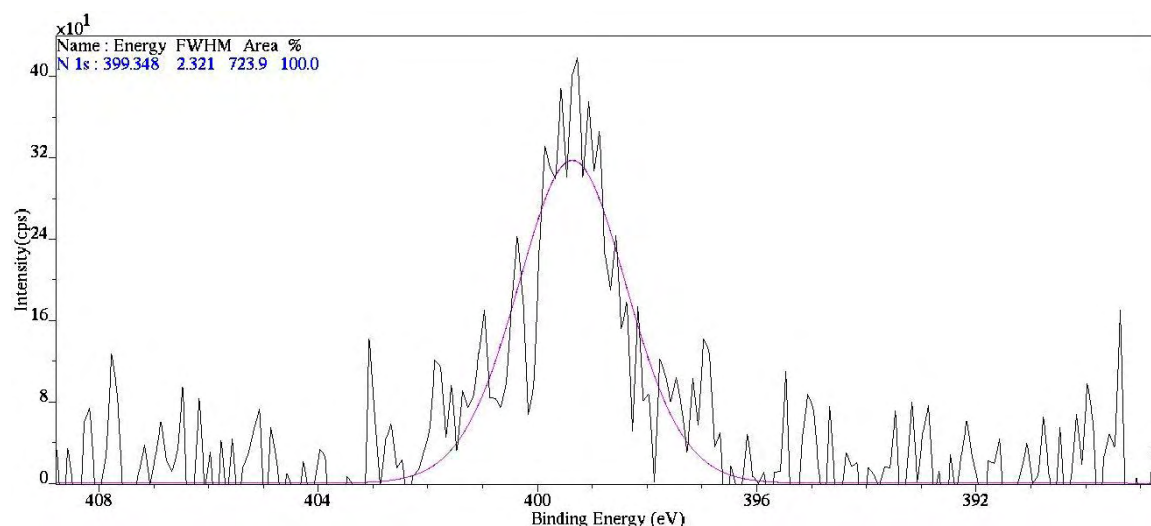
Figure 43 : N-1s HR peak deconvolution

Si, S, Mo, Ca and Cl provided peaks with low intensity, unable to be fitted for qualitative results. On the contrary, Mn, Ni and Co did not been detected.

4.5.2 Area with spots

The analysis in this area, provided a few differences in comparison with the previous case.

Carbon, except the lower *1s* peak intensity, meaning lower percentage atomic concentration (expose contamination), provided double peak contribution for the C-C and C-O-C bonds, at 284.6eV and 285.9eV respectively. In other words, the C=O bond is missing here. The lower C concentrations connected to the O *-1s* peak deconvolution, where in this case the results regarding the metal-oxides/carbon-oxides ratios are presented increased about 5:14, while in the previous case (Figs. 37 and 38) were less than 2:9.
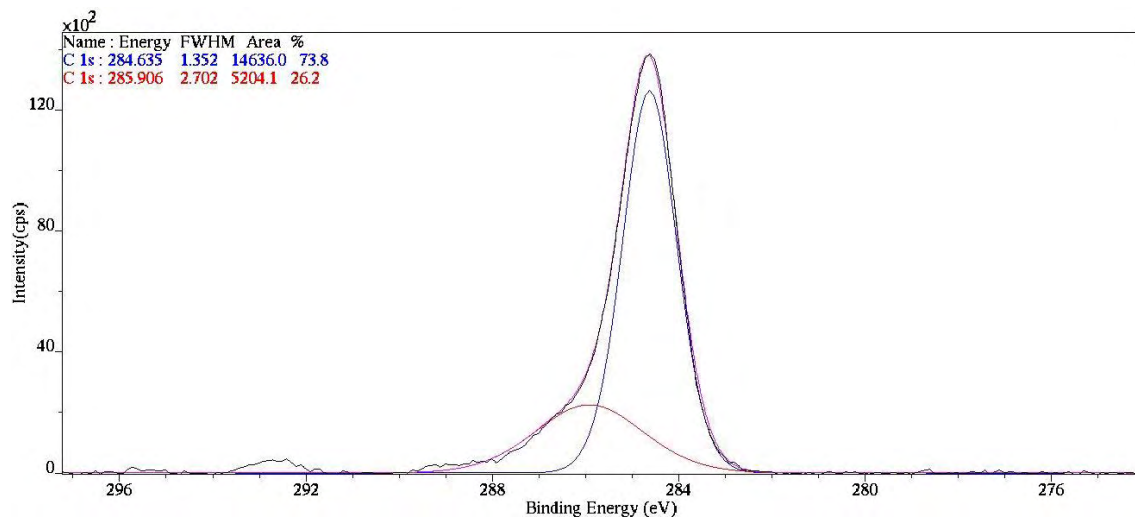
Figure 44 : C-1s HR peak deconvolution
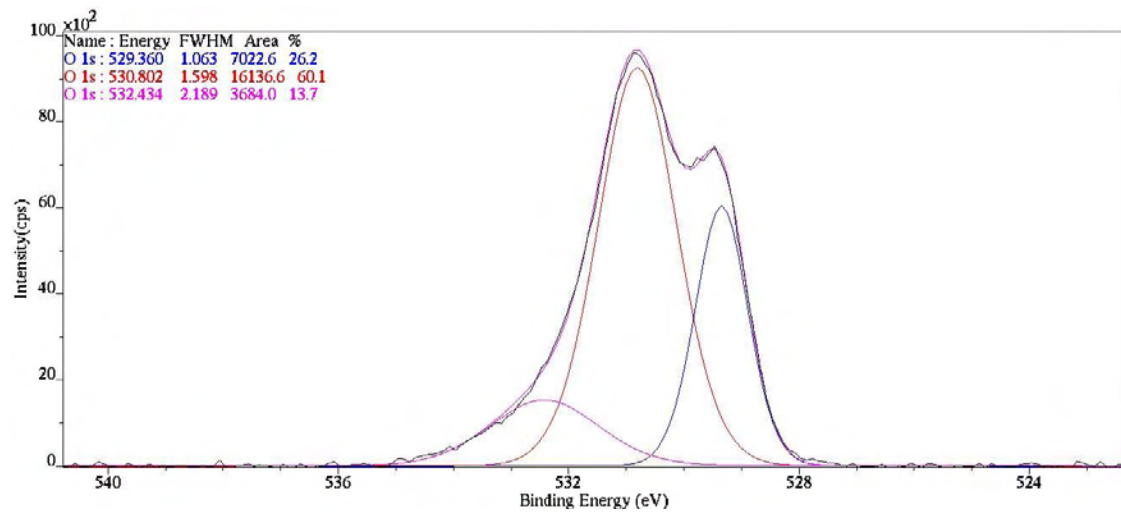
Figure 45 : O-1s HR peak deconvolution

Despite the increasing in metal oxides, the spots include metallic Fe (Fe^0 -$2p_{3/2}$ orbital with 706.8eV of binding energy together with the same oxidation states (709.2eV Fe^{+2} and 711.9eV for the Fe^{+3}) of the metal. The Fe^0/Fe-oxides ratio was calculated at around 4:21.
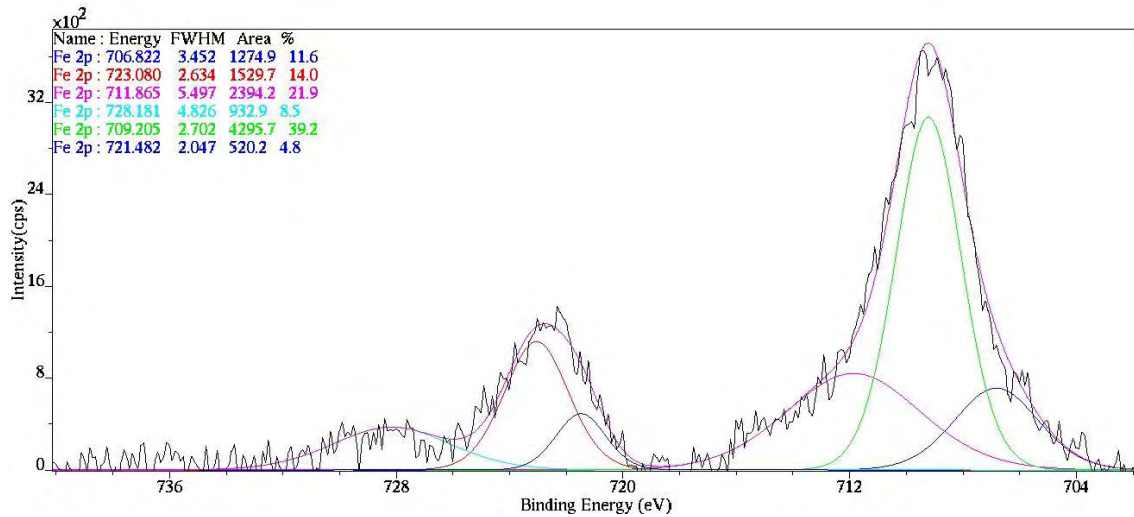
Figure 46 : Fe-1s HR peak deconvolution

For Cr the received *2p* peaks remained identical and no important changes for metallic and oxidized percentage concentrations were recorded, as Fig. 47 shows in comparison with Fig. 40.
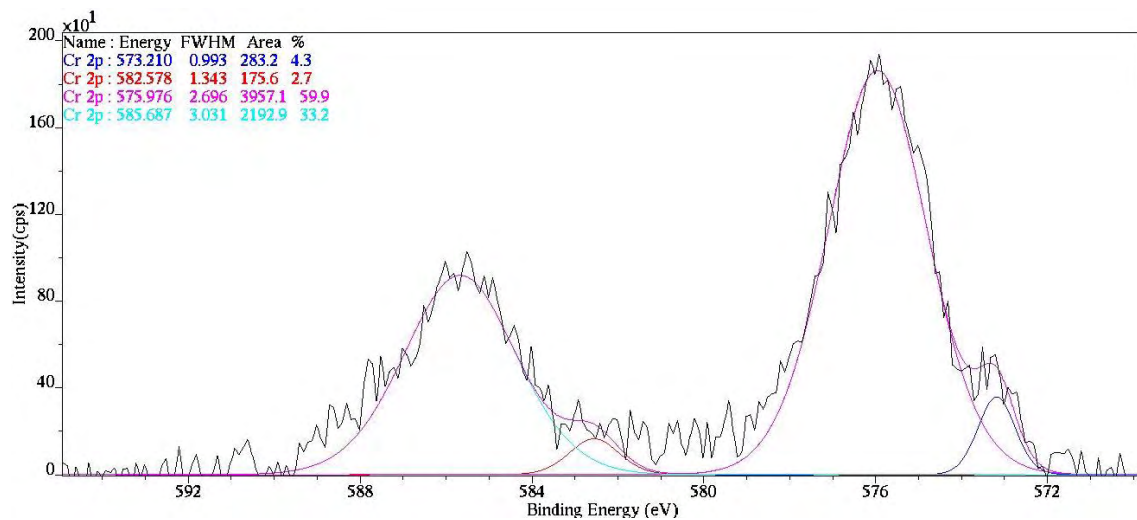
Figure 47 : Cr-1s HR peak deconvolution

Significant difference in P were recorded after the *2p* peak deconvolution of the element from the spot area (Fig. 48). The peaks were formed in higher binding energies at 132.7eV and 133.5eV for the $2p_{3/2}$ and $2p_{1/2}$ respectively, shifted by 0.4eV (important shift as the error is about 0.2eV) revealing that the element remains again at the P-O ionic state, but in this case it does not participate in the bond with metal [34], and possibly is connected with carbon and hydrogen (C-H-P-O) [35].
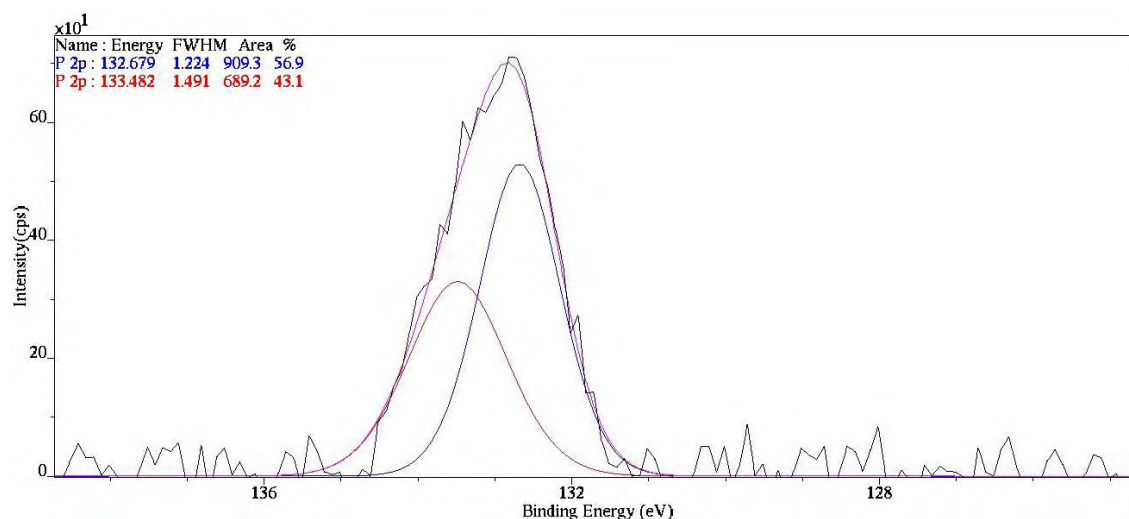
Figure 48 : P-1s HR peak deconvolution

Another change was detected on the Na *-1s* peak position. In the specific analysis area, N *-1s* peak is centered at 1071eV, in contrast with the typical Na^+ peak, which here emerge from the Na-C bond [36], [37] or/and the bond of the element with Mo [38]. The last assertion is reinforced by the Mo peaks, which now are presented with higher intensity and thus, the fitting process completed successfully (Fig. 50). The Mo *-3d$_{5/2}$* orbitals revealed both the Mo^0 electronic state (metallic) at 227.2eV [39], [40] and the Mo^{+5} at 231.8eV [40–42].
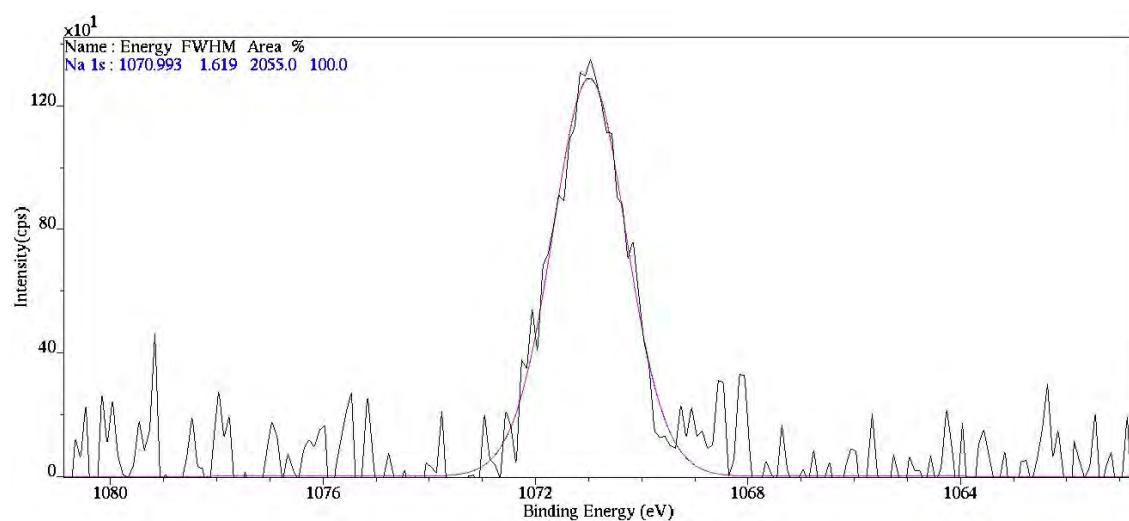
Figure 49 : Na-1s HR peak deconvolution
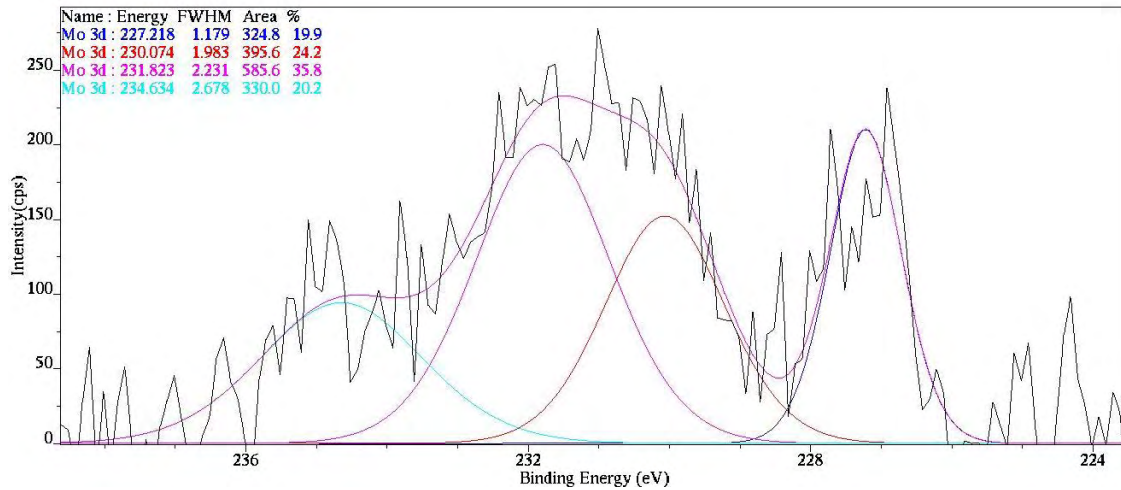
Figure 50 : Mo-1s HR peak deconvolution

N *-1s* peak has alterations too. The orbital was centered at much lower binding energy (337.7eV) in comparison with the previous case. This shift is typical when N is connected with metals [43], to form bonds in a metallic matrix, for example with Si [44], [45].
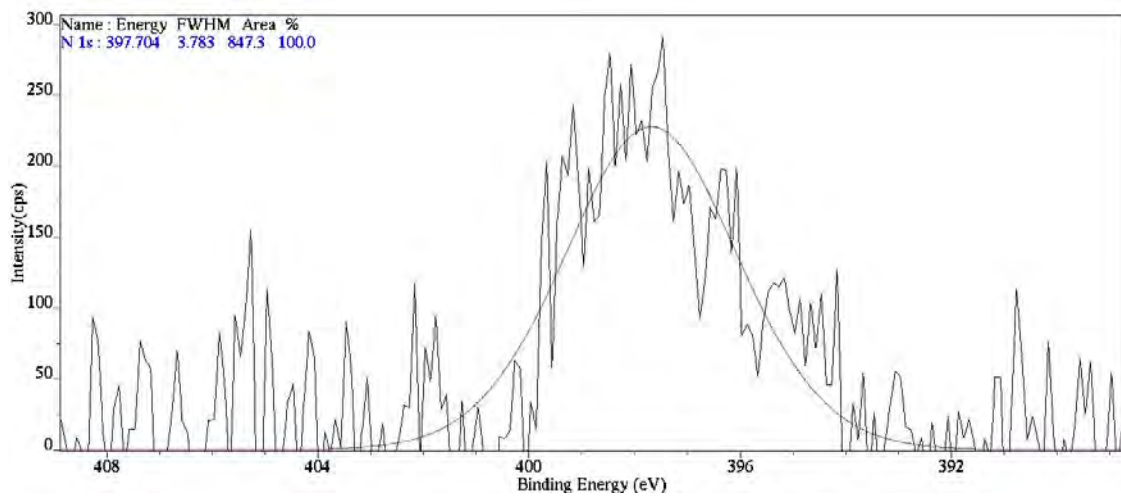
Figure 51 : N-1s HR peak deconvolution

Finally, in this analysis surface region, the intensity from the Ca collected photoelectrons provided higher peak intensity (Fig. 52). The Ca *-2p3/2* orbitals were recorded with binding energy at around 347eV, for the Ca-O bond and probably for the $CaCO_3$ compound.
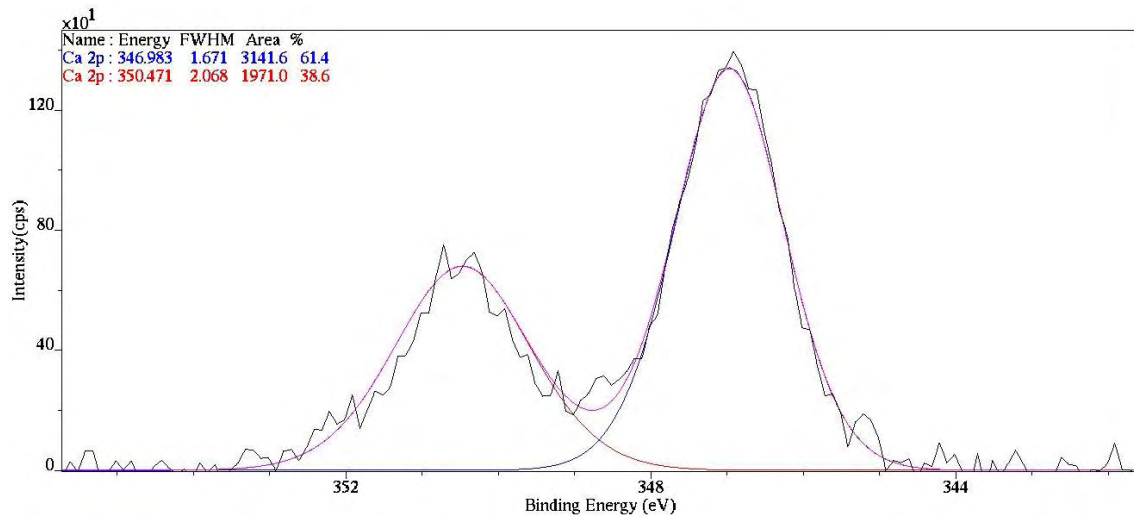
Figure 52 : Ca-1s HR peak deconvolution

On the specific position of the sample's surface (spot), Si and Cl provided too low intensity to be fitted, while none from the S, Mn, Ni, Co elements were detected.

Chapter 5 : Conclusions & Discussion

5.1 Corrosion Mechanism

Taking into consideration the results presented in Chapter 4, the main findings can be summarized as follows :

According to the polarization curves, the specimen started to oxidize at potentials nobler than the corrosion potential E_{corr}. This stage is succeeded by the passivation stage. As the current density increases, the passivation stage is completed at a potential value, where the passive film (Cr-O) has been dissolved. The negative hysteresis loop indicates the susceptibility of the material to pitting corrosion.

Examination of the microstructure revealed a differentiation in the corrosion resistance behavior of the two phases (ferrite and austenite). By observing the transverse cross-section area close to a pit, the ferritic phase seemed to be in smaller content compared to austenitic in a region near the edge of the pit. This behavior is explained by the fact that ferrite plays the role of anode while austenite is the cathode. This galvanic corrosion evolves into pitting corrosion.

SEM/EDX analyses indicated a significant reduction of Cr content inside the pits in the surface of the specimen, and close to edge of pits in transverse cross-section as well.

It was noticed that despite the significant corrosion behavior, according to the polarization tests, of the hyper-duplex stainless steel 2707, pitting corrosion was found through the optical microscopy and SEM/EDX analysis. It is possible that during the polarization tests, in the cathodic region, the phenomenon which is represented to be hydrogen corrosion. This hypothesis can be examined by avoiding such low potential values during the cathodic part in future tests. So the potential range could reach values -1000 mV below the E_{rest}.

Summarizing, the two phases exhibit significantly different corrosion behavior. Both phases are initially protected by a Cr-rich film, but ferrite start to be corroded at lower potential values than austenite. With increase of potential, corrosion evolves towards to the boundaries of the two phases and also austenite start to be corroded at higher potential values. This point corresponds to the breakdown potential E_b in the polarization curves.

5.2 Products of Corrosion and Depth of Pits

XPS results indicated an increase of the metal-oxides/carbon-oxides ratio in the area, where pits were formed, compared to the clear surface. As far as Cr, it has been oxidized and Cr_2O_3 was formed. The oxidized/metallic ratio for Cr is 23:2. In the area where pits were encountered, Fe has been oxidized and the oxidation states that appear are Fe^{2+} and Fe^{+3}. Also, the Fe^0/Fe-oxides ratio was calculated at around 4:21.

It is important to mention that the most severe pit reached a depth of approximately 38 μm. Concerning that the thickness of the as-received tube was 2 mm, the maximum depth of a pit was 1,9 % of the thickness of the tube.

5.3 Future Work Recommendations

As an extension of this study, Raman spectroscopy could be used for the in-depth characterization of the products formed during corrosion.

One possible future study could include the interruption of the cyclic potentiodynamic polarization tests in specific potential values and the further comparative examination of each condition through metallographic, EDX/SEM and XPS analysis.

Also, investigation of annealing and aging conditions could contribute to balancing PREN values of ferrite and austenite and thus avoid the problems caused by selective dissolution.

Conduction of cyclic potentiodynamic anodic polarization could provide more detailed information on the repassivation ability of the steel.

Finally, conduction of cyclic potentiodynamic polarization test in temperatures higher than 25°C, having the critical pitting temperature (CPT) into consideration, could provide useful information for the corrosion resistance of the 2707 steel.

References

[4]   Sandvik Group - Home. (n.d.). Retrieved May 5, 2018, from
         https://www.home.sandvik/en/

[5]   "BRITISH STAINLESS STEEL ASSOCIATIONMaking the Most of Stainless
         Steel." *Bssa.org.uk*, www.bssa.org.uk/about_stainless_steel.php?id=31.

[6]   *Practical Guidelines for the Fabrication of Duplex Stainless Steels*. 3rd ed.,
         IMOA, 2009.

[7]   Millet, F., Friez, P., Franzi, A., Bonnefois, B., & Lardon, J. (1996). Superduplex
         Stainless Steel Use in Manufacturing Highly Sour Gas Centrifugal
         Compressors. *Volume 3: Coal, Biomass and Alternative Fuels; Combustion
         and Fuels; Oil and Gas Applications; Cycle Innovations*. doi:10.1115/96-gt-
         272

[8]   Tiziano Bellezze, Giampaolo Giuliani, Gabriella Roventi. *Study of stainless
         steels corrosion in a strong acid mixture. Part 1: cyclic potentiodynamic
         polarization curves examined by means of an analytical method,* Corrosion
         Science, 2018.

[9]   Tiziano Bellezze, Giampaolo Giuliani, Annamaria Viceré, Gabriella Roventi,
         *Study of stainless steels corrosion in a strong acid mixture. Part 2: anodic
         selective dissolution, weight loss and electrochemical impedance
         spectroscopy tests*, Corrosion Science, 2018.

[10]   Guocai Chaii & Pasi Kangas, *RECENT DEVELOPMENTS OF ADVANCED
         AUSTENITIC AND DUPLEX STAINLESS STEELS FOR OIL AND GAS
         INDUSTRY*, 2014.

[11]   J.-O. Nilsson, G. Chai, U. Kivisäkk, *RECENT DEVELOPMENT OF DUPLEX
         STAINLESS STEELS.*

[12]   Soon-Hyeok Jeon, Soon-Tae Kim, Se-Young Kim, Min-Seok Choi and Yong-
         Soo Park, *Effects of Solution-Annealing Temperature on the Precipitation of
         Secondary Phases and the Associated Pitting Corrosion Resistance in Hyper
         Duplex Stainless Steel,* Materials Transactions, Vol. 54, No. 8 (2013) pp.
         1473 to 1479 ©2013 The Japan Institute of Metals and Materials.

[13]   A.J. Bard and L.R. Faulkner, *Electrochemical Methods*, Wiley, 1980

[14]   D.A. Jones, *Principles and prevention of corrosion*, Macmillan Publishing Company, 1992

[15]   A. Lekatou, *Corrosion and protection of metals in plain terms*, Rethymno, Nimertis Editions, 2013, p. 104-107, 285-288.

[16]   Jinshan Pan & Christofer Leygraf, *In Situ Local Dissolution of Duplex Stainless Steels in 1 M H 2 SO 4 + 1 M NaCl by Electrochemical Scanning Tunneling Microscopy,* 2002.

[17]   E.A.M. Hussain, M.J. Robinson, *Erosion–corrosion of 2205 duplex stainless steel in flowing seawater containing sand particles,* 2006.

[18]   Chambers, B., Srinivasan, S., Yap, K. M., & Yunovich, M.. *Corrosion In Crude Distillation Unit Overhead Operations: A Comprehensive Review*. NACE International, (2011, January 1).

[19]   T. Zhang, X. Meng, Z. He, Y. Lin, X. Liu, D. Li, J. Li, X. Qiu, Preparation of Magnetic Nanoparticles via a Chemically Induced Transition: Role of Treating Solution's Temperature, Nanomaterials. 7 (2017) 220. doi:10.3390/nano7080220.

[20]   L.Q. Guo, B.J. Yang, D. Liang, L.J. Qiao, Surface preparation effect on duplex stainless steel passive film electrical properties studied by in situ CSAFM, J. Mater. Res. 30 (2015) 3084–3092. doi:10.1557/jmr.2015.245.

[21]   S. Oida, F.R. McFeely, A.A. Bol, X-ray photoelectron spectroscopy study on Fe and Co catalysts during the first stages of ethanol chemical vapor deposition for single-walled carbon nanotube growth, J. Appl. Phys. 109 (2011) 064304. doi:10.1063/1.3552306.

[22]   R. Wang, W. Yang, Y. Song, X. Shen, J. Wang, X. Zhong, S. Li, Y. Song, A General Strategy for Nanohybrids Synthesis via Coupled Competitive Reactions Controlled in a Hybrid Process, Sci. Rep. 5 (2015) 9189. doi:10.1038/srep09189.

[23]   D. Chandra, R. Tsuriya, T. Sato, D. Takama, N. Abe, M. Kajita, D. Li, T. Togashi, M. Kurihara, K. Saito, T. Yui, M. Yagi, Characterization of Interfacial Charge-Transfer Photoexcitation of Polychromium-Oxo-Electrodeposited TiO 2 as an Earth-Abundant Photoanode for Water Oxidation Driven by Visible Light, Chempluschem. 81 (2016) 1116–1122. doi:10.1002/cplu.201600288.

[24]   T. Nishimura, Structure of the Passive Film formed on Fe&ndash;Mn&ndash;Si&ndash;Cr&ndash;Ni Shape Memory Alloy after Wet and Dry Corrosion Test, Mater. Trans. 55 (2014) 871–876. doi:10.2320/matertrans.M2014029.

[25] J. Peng, K. Lu, S. Hu, Z. Fang, H. Ning, J. Wei, Z. Zhu, Y. Zhou, L. Wang, R. Yao, X. Lu, High Conductivity and Adhesion of Cu-Cr-Zr Alloy for TFT Gate Electrode, Appl. Sci. 7 (2017) 820. doi:10.3390/app7080820.

[26] Z. Qiang, Y. Xia, X. Xia, B.D. Vogt, Generalized Synthesis of a Family of Highly Heteroatom-Doped Ordered Mesoporous Carbons, Chem. Mater. 29 (2017) 10178–10186. doi:10.1021/acs.chemmater.7b04061.

[27] Z. Wang, W. Wu, The tribological properties of the polyurea greases based on oil-miscible phosphonium-based ionic liquids, Lubr. Sci. 30 (2018) 16–22. doi:10.1002/ls.1391.

[28] N. Díez, A. Śliwak, S. Gryglewicz, B. Grzyb, G. Gryglewicz, Enhanced reduction of graphene oxide by high-pressure hydrothermal treatment, RSC Adv. 5 (2015) 81831–81837. doi:10.1039/C5RA14461B.

[29] J. Zou, Y. Dai, K. Pan, B. Jiang, C. Tian, G. Tian, W. Zhou, L. Wang, X. Wang, H. Fu, Recovery of silicon from sewage sludge for production of high-purity nano-SiO2, Chemosphere. 90 (2013) 2332–2339. doi:10.1016/j.chemosphere.2012.10.087.

[30] A. Hu, R. Liang, X. Zhang, S. Kurdi, D. Luong, H. Huang, P. Peng, E. Marzbanrad, K.D. Oakes, Y. Zhou, M.R. Servos, Enhanced photocatalytic degradation of dyes by TiO2 nanobelts with hierarchical structures, J. Photochem. Photobiol. A Chem. 256 (2013) 7–15. doi:10.1016/j.jphotochem.2013.01.015.

[31] C. Wei, C. Cheng, S. Wang, Y. Xu, J. Wang, H. Pang, Sodium-Doped Mesoporous Ni 2 P 2 O 7 Hexagonal Tablets for High-Performance Flexible All-Solid-State Hybrid Supercapacitors, Chem. - An Asian J. 10 (2015) 1731–1737. doi:10.1002/asia.201500335.

[32] S.J. Kerber, J.J. Bruckner, K. Wozniak, S. Seal, S. Hardcastle, T.L. Barr, The nature of hydrogen in x-ray photoelectron spectroscopy: General patterns from hydroxides to hydrogen bonding, J. Vac. Sci. Technol. A Vacuum, Surfaces, Film. 14 (1996) 1314–1320. doi:10.1116/1.579947.

[33] S. Lu, X. Zhao, S. Zhu, Y. Song, B. Yang, Novel cookie-with-chocolate carbon dots displaying extremely acidophilic high luminescence, Nanoscale. 6 (2014) 13939–13944. doi:10.1039/C4NR03965C.

[34] M. Tabbal, P. Mérel, S. Moisa, M. Chaker, E. Gat, A. Ricard, M. Moisan, S. Gujrathi, XPS and FTIR analysis of nitrogen incorporation in CNx thin films, Surf. Coatings Technol. 98 (1998) 1092–1096. doi:10.1016/S0257-8972(97)00229-6.

[35] I.N. Shabanova, F.F. Chausov, E.A. Naimushina, N. V. Somov, XPS characterization of new corrosion inhibitor: zinc aminophosphonate coordination complex, Surf. Interface Anal. 46 (2014) 750–753. doi:10.1002/sia.5479.

[36] S. SUZUKI, K. ABIKO, H. KIMURA, Chemical State of Phosphorus Segregated

at Grain Boundaries in Iron, Trans. Iron Steel Inst. Japan. 23 (1983) 746–751. doi:10.2355/isijinternational1966.23.746.

[37] S. Wu, W. Wang, M. Li, L. Cao, F. Lyu, M. Yang, Z. Wang, Y. Shi, B. Nan, S. Yu, Z. Sun, Y. Liu, Z. Lu, Highly durable organic electrode for sodium-ion batteries via a stabilized α-C radical intermediate, Nat. Commun. 7 (2016) 13318. doi:10.1038/ncomms13318.

[38] E. Verveniotis, Y. Okawa, M. V. Makarova, Y. Koide, J. Liu, B. Šmíd, K. Watanabe, T. Taniguchi, K. Komatsu, T. Minari, X. Liu, C. Joachim, M. Aono, Self-assembling diacetylene molecules on atomically flat insulators, Phys. Chem. Chem. Phys. 18 (2016) 31600–31605. doi:10.1039/C6CP06749B.

[39] Z. Zhang, R. Yang, Y. Gao, Y. Zhao, J. Wang, L. Huang, J. Guo, T. Zhou, P. Lu, Z. Guo, Q. Wang, Novel Na2Mo4O13/α-MoO3 hybrid material as highly efficient CWAO catalyst for dye degradation at ambient conditions, Sci. Rep. 4 (2015) 6797. doi:10.1038/srep06797.

[40] Y. Wang, F. Gao, W.T. Tysoe, Interaction of molybdenum hexacarbonyl with metallic aluminum at high temperatures: Carbide and alloy formation, J. Mol. Catal. A Chem. 236 (2005) 18–31. doi:10.1016/j.molcata.2005.03.038.

[41] M. Xiang, J. Zou, CO Hydrogenation over Transition Metals (Fe, Co, or Ni) Modified K/Mo 2 C Catalysts, J. Catal. 2013 (2013) 1–5. doi:10.1155/2013/195920.

[42] S. Wang, L.N. Bai, H.M. Sun, Q. Jiang, J.S. Lian, Structure and photocatalytic property of Mo-doped TiO2 nanoparticles, Powder Technol. 244 (2013) 9–15. doi:10.1016/j.powtec.2013.03.054.

[43] X. Zhu, J. Shen, B. Ge, X. Zhang, L. Yu, C. Nie, Research on Conductivity Property of Single Crystal Mo 2 C Thin Film with Large Surface Area, (2017) 2–7. doi:10.12783/dtmse/icmsea/mce2017/10785.

[44] M. Mishra, S. Krishna TC, P. Rastogi, N. Aggarwal, A.K.S. Chauhan, L. Goswami, G. Gupta, New Approach to Clean GaN Surfaces, Mater. Focus. 3 (2014) 218–223. doi:10.1166/mat.2014.1168.

[45] C.L. Cha, E.F. Chor, Y.M. Jia, A.J. Bourdillon, H. Gong, J.S. Pan, A.Q. Zhang, S.K. Tang, C.B. Boothroyd, Evaluation of silicon nitride and silicon carbide as efficient polysilicon grain-growth, J. Mater. Sci. Lett. 18 (1999) 1427–1431. doi:10.1023/A:1006679625601.

[46] A. Radi, K.T. Leung, Competitive Bonding of Amino and Hydroxyl Groups in Ethanolamine on Si(100)2×1: Temperature-Dependent X-Ray Photoemission and Thermal Desorption Studies of Nanochemistry of a Double-Chelating Agent, Mater. Express. 1 (2011) 144–153. doi:10.1166/mex.2011.1015.